# UC San Diego
## UC San Diego Electronic Theses and Dissertations

**Title**
The evolution of Western Pacific mantle lithosphere inferred from Aitutaki xenoliths

**Permalink**
https://escholarship.org/uc/item/7qt1z8q5

**Author**
Snortum, Eric Gregory

**Publication Date**
2018

Peer reviewed|Thesis/dissertation

UNIVERSITY OF CALIFORNIA SAN DIEGO

# The evolution of Western Pacific mantle lithosphere inferred from Aitutaki xenoliths

A thesis submitted in partial satisfaction of the
requirements for the degree Master of Science

in

Earth Sciences

by

Eric Snortum

Committee in charge:

    James M.D. Day, Chair
    Emily Chin
    Geoffrey W. Cook

2018

The thesis of Eric Snortum is approved, and it is acceptable

in quality and form for publication on microfilm and electronically:

_____

_____

_____

University of California San Diego

2018

TABLE OF CONTENTS

LIST OF FIGURES

LIST OF TABLES

ACKNOWLEDGEMENTS

ABSTRACT OF THE THESIS


# The evolution of Western Pacific mantle lithosphere inferred from Aitutaki xenoliths


by

Eric Snortum

Master of Science in Earth Sciences

University of California San Diego, 2018

Dr. James M.D. Day, Chair



A suite of mantle xenoliths from Aitutaki, which forms part of the Cook-Austral hotspot chain, have been examined for highly siderophile element (HSE: Os, Ir, Ru, Pt, Pd, Re) abundances and Re-Os isotope systematics to investigate the compositional nature of Western Pacific mantle lithosphere. These data are complemented by olivine mineral analyses and whole-rock major and trace element abundances. The Aitutaki xenolith suite comprises low-Al dunite, harzburgite, and lherzolite, and high-Al olivine websterite, and pyroxenite lithologies. The xenolith suite is hosted within Aitutaki nephelinite lavas representing low degree (<1%) partial melts from an enriched mantle (EM1/EM2) source ($^{187}Os/^{188}Os = \sim0.136$). High-Al xenoliths have experienced significant melt-rock interaction with melts similar in composition to the lavas that host the xenoliths, with pyroxenites having similar HSE abundances and Os isotope compositions to the lavas ($Al_2O_3 = $ 5.7-8.3 wt.%; $^{187}Os/^{187}Os = 0.1263$ to $0.1469$). Conversely, Aitutaki lherzolites and harzburgites are similar in composition to abyssal peridotites with respect to their $^{187}Os/^{188}Os$ ratios (0.1264

±43), HSE and major element abundances (MgO and $Al_2O_3$), forsterite content, and typical extents of melt depletion (~10 to 14 %). Aitutaki xenolith compositions would lead to the conclusion of a relatively fertile lherzolitic lithospheric mantle. The geochemical evidence for pervasive melt infiltration, however, suggests that Pacific oceanic plate mantle lithosphere is more depleted than previously thought. The results show that extensive and recent melt-rock reaction is superimposed on both recent melting at the ridge and prior melt depletion evident from Mesoproterozoic time of rhenium depletion ages (~1.5 Ga) in some Aitutaki xenoliths. Similar evidence for melt refertilization superimposed on Proterozoic melt depletion ages are exhibited in xenoliths from the Samoan islands of Savai'i and Tubuai, implying that a wide region of the Western Pacific oceanic mantle lithosphere preserves evidence for extensive melt-depletion in the Mesoproterozoic.

## 1.1. Introduction

 The composition of Earth's mantle is key in understanding processes in terrestrial evolution, including the total heat budget, as well as the surficial expression of the outer-most layer, the lithosphere, and its physical properties. Relatively minor variations in chemical composition within the mantle have been attributed to large effects including response to physical stress and buoyancy (e.g. Karato, 1986; Hirth and Kohlstedt, 1996; Afonso et al., 2007; Simon et al., 2008). Lithospheric mantle composition is also likely to be important in generation of melts at the lithosphere/asthenosphere boundary and, ultimately, after subduction zone recycling (e.g., Zindler & Hart, 1986). Contributing to our understanding of the lithospheric oceanic mantle are abyssal peridotites found at mid-ocean ridges and fracture zones (e.g., Warren, 2016), and mantle xenoliths found at ocean islands (Simon et al., 2008).

 Ocean island hotspot tracks allow the opportunity for glimpses into mantle compositions from peridotite and pyroxenite xenoliths brought to the surface by their host lavas. Along their journey to the surface, these melts can react with the original rock at depth and change the lithology of what will eventually become xenoliths (Keleman et al., 1992). It has been shown that melt-rock reaction can fundamentally change basalts forming at mid-ocean ridges (Lissenberg et al., 2008) and form podiform chromitites in the upper mantle (Zhou et al., 1994), both of which are large-scale processes that influence the physical properties of the Earth significantly.

 Evidence suggests that the oceanic crust is underlain by melt-depleted peridotite (Johnson et al., 1990), yet there is still uncertainty on large scales, such as entire ocean basins, as to what degree these peridotites have been depleted. Generally, it appears that the Pacific plate is relatively homogenous but can contain old depleted mantle domains (Lassiter et al., 2014; Day et al., 2017). However, the ability to sample the Pacific oceanic lithosphere is limited by fast-spreading, leading to few exposures at transform faults or tectonic features, such as mega-mullions, as are the case for slower spreading oceanic plate. Mantle convection times are on the order of 50 to 200 Ma (Zhong et al., 2005) and it has been shown that over multiple mantle convection cycles strongly depleted peridotite can remain relatively undisturbed and even cluster to form larger heterogeneities within the mantle (Manga, 1996). This suggests that the oceanic crust could be sitting atop larger areas of extremely depleted (up to 20 %) upper mantle.

In this study, I investigated xenoliths from Aitutaki. Aitutaki is an ocean island found in the South Pacific at the north-west end of the Cook-Austral hotspot track (***Figure 1***). The xenoliths offer the opportunity to investigate oceanic mantle in a poorly sampled region of the Western Pacific, with the nearest studied mantle xenoliths being over 1000 km away, with two goals. The first was to examine the nature of Pacific mantle lithosphere and melt-rock reactions with ocean island basalt melts. The second goal was to examine the degree of melt depletion in the Western Pacific lithosphere and to compare these data with ocean island mantle xenoliths from Samoa and with abyssal peridotites.
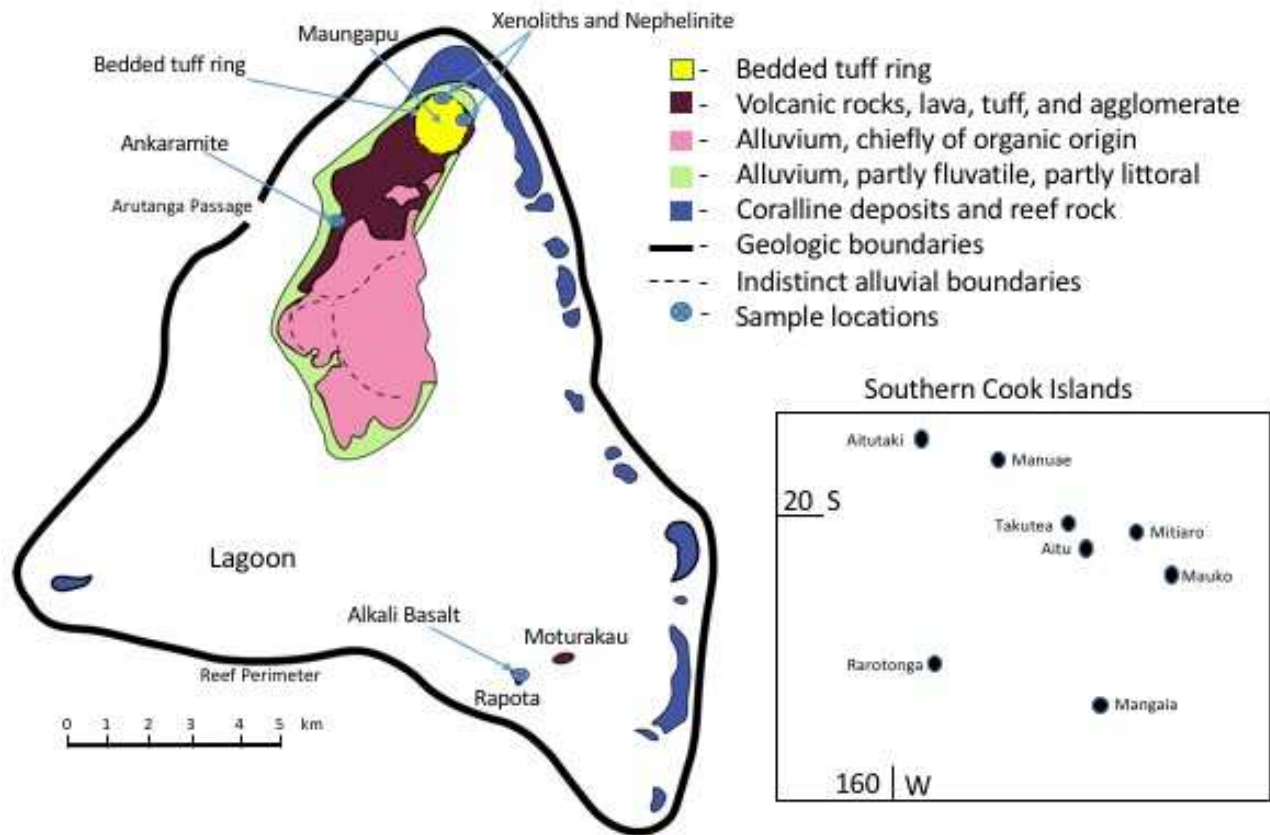


**Figure 1:** Geologic map of Aitutaki, Southern Cook Islands (inset) with sample locations. Geology is based on map by Wood, 1978.

# 2. Methods

In this study all whole-rock samples were measured for major- and trace-element abundances. Due to the limited available mass however, AK-1029, AK-1020, AK-1023-1, AK-1023-5, AK-1006, and AK-1005 were not measured for $^{187}Os/^{188}Os$ and HSE abundances.

## 2.1. Olivine mineral major-element analysis

Mineral major- and minor-element analyses were performed on polished one-inch rounds containing olivine grains from Aitutaki xenolith samples. Measurements were made using a *JEOL JXA-8900* electron microprobe analyser at the University of Maryland. Mineral compositions were determined in wave-length dispersive spectral mode using an acceleration potential of 15 keV, a 20 nA beam current, with the beam focused to 2 μm. Peak and background counting times were 20-30 s, and standard ZAF correction procedures were used. Natural and synthetic standards were used for calibration and were measured periodically within analytical sessions. The detection limits (3σ above background) are <0.03 wt. % for all oxides listed.

## 2.2. Whole-rock major and trace element abundance analyses

Major element compositions were measured by X-ray fluorescence (XRF) at Franklin and Marshall College using a *PW 2404 PANalytical* XRF vacuum spectrometer following the procedures outlined in Boyd & Mertzman (1987). Major element analyses by XRF involved standard lithium tetraborate fusion techniques using 3.6:0.4 g LiBO4:sample powder. Ferrous iron concentrations were determined by titration with potassium dichromate. Precision and accuracy are estimated using repeat analyses of standards, with long-term reproducibility (in wt.% and 2σ absolute standard deviation, *n* = 13) of ± 0.13 for $SiO_2$, ± 0.01 for $TiO_2$, ± 0.09 for $Al_2O_3$, ± 0.63 for FeO, ± 0.47 for $Fe_2O_3$, ± 0.10 for $Fe_2O_3^T$, ± 0.01 for MnO, ± 0.04 for MgO, ± 0.07 for CaO, ± 0.03 for $Na_2O$, ± 0.01 for $K_2O$, and ± <0.01 for $P_2O_5$. Accuracy for the average of 13 runs of BHVO-2 relative to USGS values is better than 0.2% for $SiO_2$ and $TiO_2$, <1% for $Al_2O_3$, MgO, $Fe_2O_3T$, CaO, $Na_2O$, $P_2O_5$, and <3% for $K_2O$ (Day et al., 2017).

Trace-element abundances were determined at the *Scripps Isotope Geochemistry Laboratory* (*SIGL*), Scripps Institution of Oceanography using methods described previously (Day et al., 2014) and can be found in ***Table 1***. One hundred milligrams of powder was precisely weighed and digested in a 1:4 mixture of Teflon-distilled $HNO_3$:HF for >72 Hrs at 150˚C on a hotplate. Rock standards (BHVO-2, BIR-1, HARZ-01) and total procedural blanks were prepared with samples. After drying down and sequential $HNO_3$ dry-down steps to break-down fluorides, clear sample solutions, free of any solid material, were diluted by a factor of 5000 in 2% $HNO_3$ and doped with a 1 ppb In solution to monitor instrumental drift. Solutions were measured using a *Thermo Scientific* iCAPq c quadrupole inductively coupled plasma mass spectrometer at the *SIGL*. Reproducibility of the reference materials was generally better than 5% (RSD) for basaltic and peridotite standards, and element abundances were generally within error of recommended values (see Day et al., 2017).

## 2.3. Highly siderophile element abundances and $^{187}Os/^{188}Os$ ratios

Osmium isotope and HSE abundance analyses were performed at the *SIGL*. Precisely weighed homogenised powders were digested in sealed borosilicate Carius tubes with isotopically enriched multi-element spikes ($^{99}Ru$, $^{106}Pd$, $^{185}Re$, $^{190}Os$, $^{191}Ir$, $^{194}Pt$), and 12 mL of a 1:2 mixture of multiply Teflon distilled HCl and $HNO_3$ purged of excess Os by repeated treatment and reaction with $H_2O_2$. Samples were digested to a maximum temperature of 270˚C in an oven for 72 hours. Osmium was triply extracted from the acid using $CCl_4$ and then back-extracted into HBr (Cohen & Waters, 1996), prior to purification by micro-distillation (Birck et al., 1997). Rhenium and the other HSE were recovered and purified from the residual solutions using standard anion exchange separation techniques (Day et al., 2016a).

Isotopic compositions of Os were measured in negative-ion mode on a *ThermoScientific* Triton thermal ionisation mass spectrometer at the *SIGL*. Rhenium, Pd, Pt, Ru and Ir were measured using an *Cetac Aridus II* desolvating nebuliser coupled to a *ThermoScientific* iCAPq c ICP-MS. Offline corrections for Os involved an oxide correction, an iterative fractionation correction using $^{192}Os/^{188}Os = 3.08271$, a $^{190}Os$ spike subtraction, and an Os blank subtraction. Precision for $^{187}Os/^{188}Os$, determined by repeated measurement of the UMCP Johnson-Matthey standard was

better than ±0.2% (2 SD; 0.11374 ±8; n = 6). Rhenium, Ir, Pt, Pd and Ru isotopic ratios for sample solutions were corrected for mass fractionation using the deviation of the standard average run on the day over the natural ratio for the element. External reproducibility for HSE analyses was better than 0.5% for 0.5 ppb solutions and all reported values are blank corrected. The total procedural blanks (*n* = 2) run with the samples gave $^{187}Os/^{188}Os$ = 0.183 ± 0.006, with quantities (in picograms) of 3 to 6 [Re], 21 [Pd], 3 [Pt], 51 to 59 [Ru], 12 to 15 [Ir] and 0.3 to 0.5 [Os]. These blanks resulted in negligible corrections to samples (<5%) except for high blank additions to AK1017L for Ir (19%) and Ru (26%), and for AK1023-8 for Re (10%). A peridotite standard, MUH-1 was run four times during the analytical campaign, and concentrations and isotopic compositions for this standard reference material are provided along with the sample data in ***Table 2***.

# 3. Results

## 3.1. Sample descriptions and olivine compositions

A total of nineteen xenoliths and three lavas from Aitutaki were examined in this study. The majority of xenolith samples are spinel lherzolites (*n* = 12; ~80% modal olivine, ~15% modal orthopyroxene, ~5% modal clinopyroxene), with singular examples of spinel dunite, spinel harzburgite, olivine clinopyroxenite, olivine pyroxenite, pyroxenite, high-$Al_2O_3$ pyroxenite, and olivine websterite. Generally, the lherzolite xenoliths appear fresh as inclusions within lavas, except for samples AK-1023-4, AK-1023-B, and AK-1023-A, all of which have patchy olivine alteration. Grain sizes for the xenoliths range from 0.1-0.5 cm in maximum dimension, in contrast to the lavas, which are aphanitic. Lava samples are nephelinites to alkali basalts, with nephelinites containing xenoliths as well as megacrysts of pyroxene and ilmenite (***Figure 2***). Visually, the lava and xenolith samples (***Figure 3***) are similar to those previously described in the only previous study of Aitutaki xenoliths, by Fodor et al. (1982). They noted that the nephelinite hosting the xenoliths is olivine-microporphyritic, with microcrystalline groundmass of olivine, clinopyroxene, magnetite-ilmenite oxides, and interstitial nepheline, whereas the lherzolite xenoliths vary in proportions of olivine, clinopyroxene and orthopyroxene, with pervasive evidence of reaction with melt.
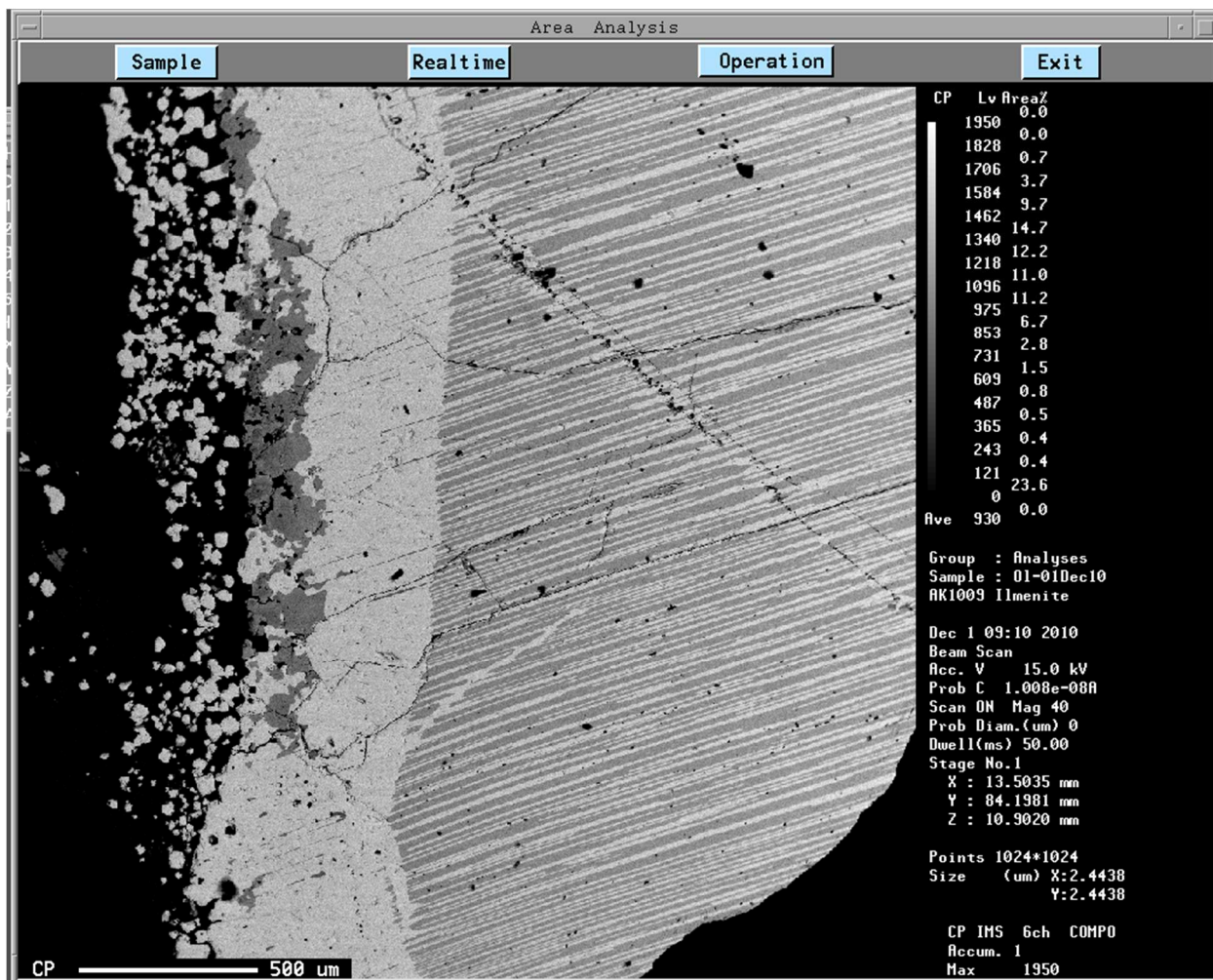
**Figure 2:** Back scatter electron image of comb-textured ilmenite megacryst in AK 1009. Scale bar is 500 microns.

**Figure 3:** Hand specimens showing evidence of melt infiltration. Lithologies are as follows: olivine websterite (AK-1028), high-Al pyroxenite (AK-1026), pyroxenite (AK-1029), and lherzolite (AK-1023-B).

Olivine compositions for Aitutaki xenoliths range from $Fo_{88}$ to $Fo_{90.9}$, with low CaO (<0.1 wt.%), and NiO that correlates with increasing Fo content. Compared with residual abyssal peridotites, olivine grains from Aitutaki xenoliths have generally lower forsterite contents (*Figure 4*).
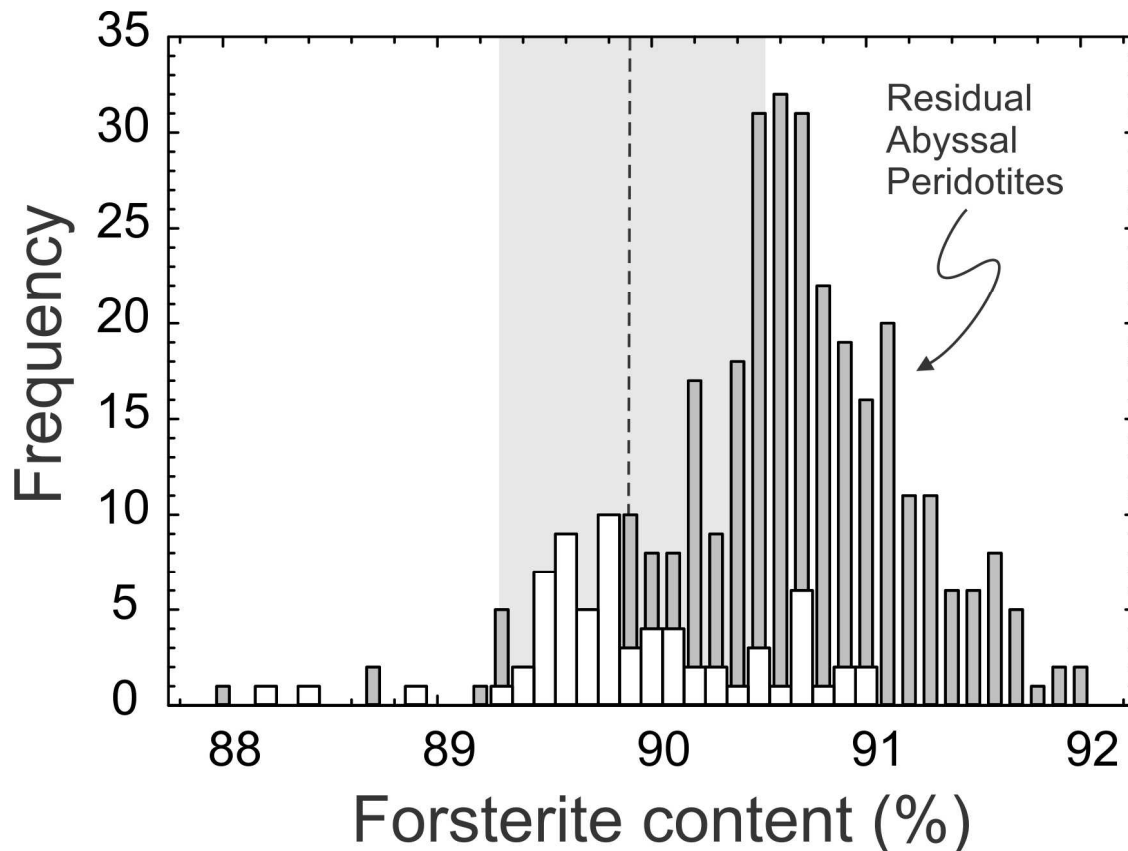
**Figure 4:** Olivine forsterite histogram of Aitutaki xenoliths (unfilled), versus residual abyssal peridotites. Aitutaki olivine compositions average $Fo_{89.9\pm0.6}$ (1SD). Residual abyssal peridotite data are from the compilation of Warren (2016).

## 3.2. Whole-rock major- and trace- element abundances

We recognize three suites of rock in this study: xenoliths with less than 5 wt. % $Al_2O_3$ (low-Al), xenoliths with greater than 5 wt. % $Al_2O_3$ (high-Al), and lavas. This distinction is made in order to separate lherzolites, dunites and harzburgites from the other recognized lithologies as seen in *Figure 5 and 6*. Xenoliths with low-Al (lherzolites, harzburgite and dunite) have similar major element compositions to residual abyssal peridotites (*Figure 5*), but the high-Al Aitutaki xenolith suite ( pyroxenites, high-Al pyroxenite and websterite) trend to more incompatible element rich compositions with decreasing MgO content. The lherzolites span a range of MgO (35.3 to 41.2 wt. %) and $Al_2O_3$ (2.08 to 4.53 wt. %), with the dunite having 46.7 wt. % MgO and 0.26 wt. % $Al_2O_3$, and the harzburgite, 41.8 wt. % MgO and 1.52 wt. % $Al_2O_3$. Concentrations of MgO (14.6 to 28.6 wt. %) are much lower and $Al_2O_3$ (5.75 to 8.91 wt. %) higher in the high-Al xenoliths. Loss on

ignition for both high- and low-Al xenoliths ranges from 0.3 to 4 wt.% and corresponds with visual evidence for limited alteration to samples.
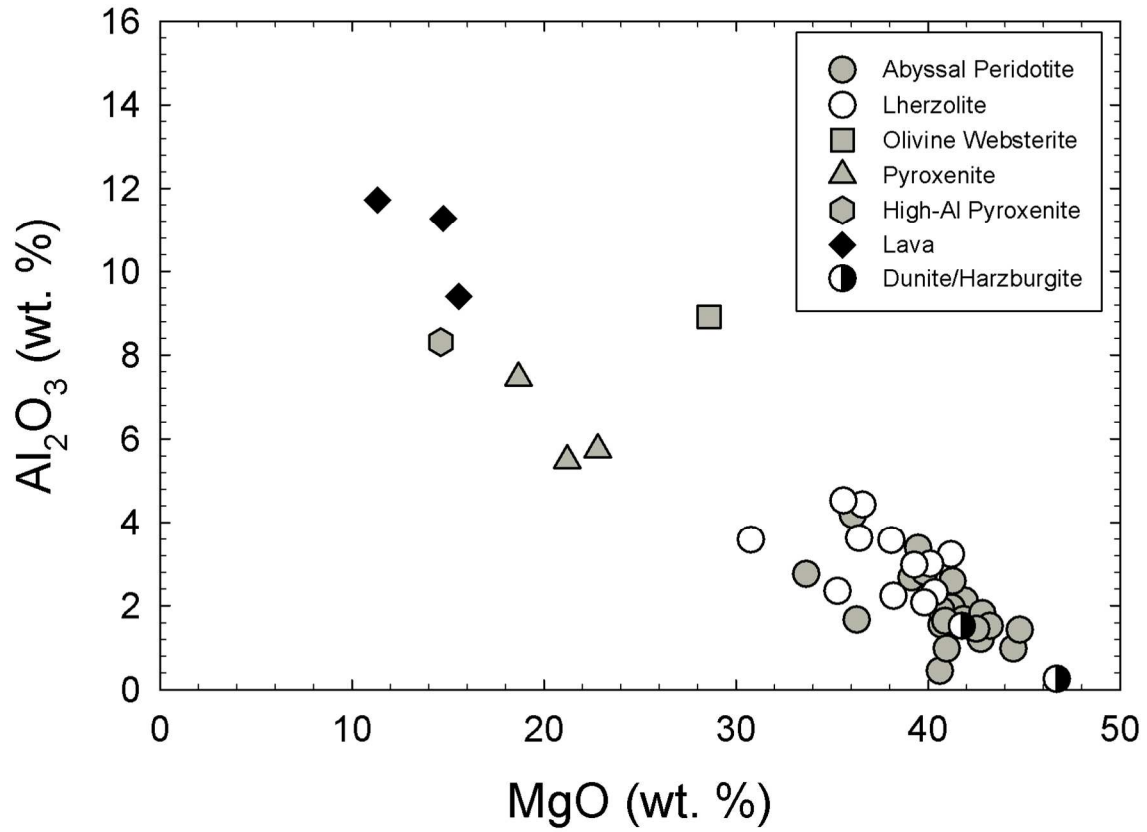


**Figure 5**: Bulk rock MgO versus $Al_2O_3$ for Aitutaki xenoliths and lavas measured in this study versus abyssal peridotite compositions from Day et al. (2017).
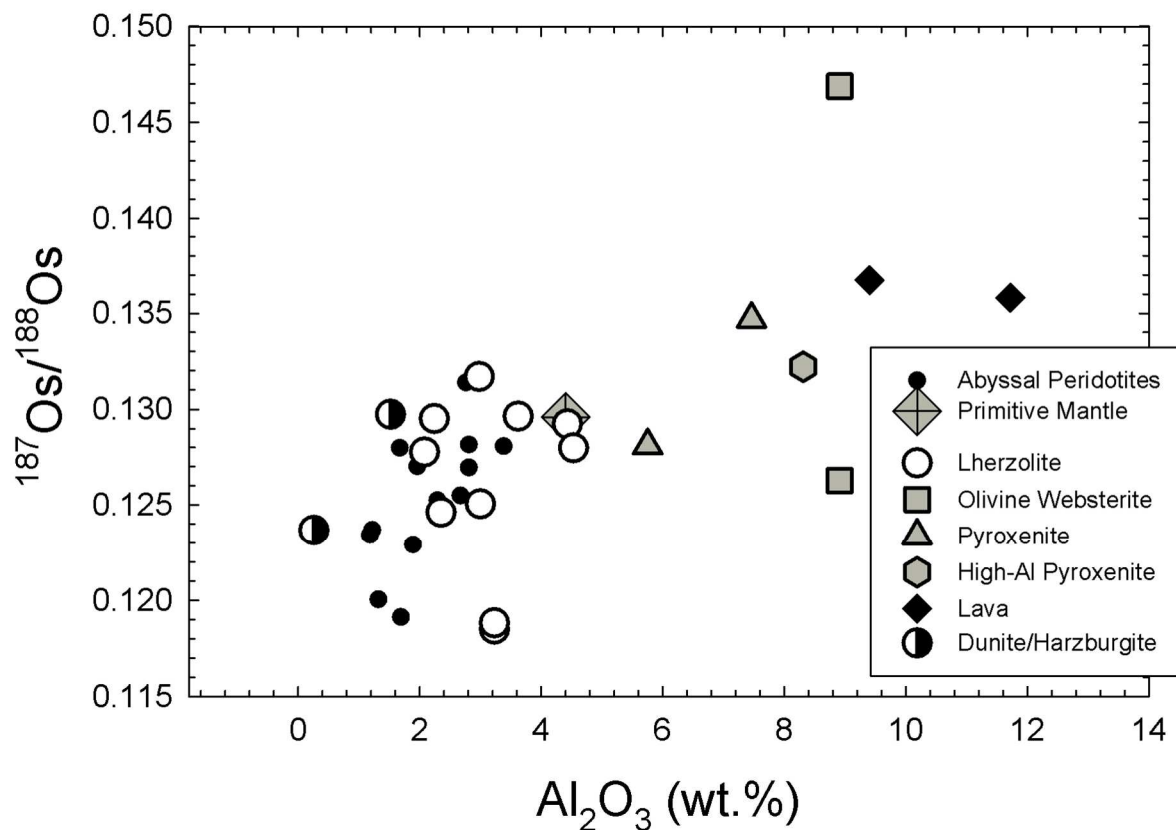
**Figure 6:** $Al_2O_3$ variation diagram for primitive mantle normalized $^{187}Os/^{188}Os$ composition for Aitutaki 'Low-Al' and 'High-Al' xenoliths and lavas measured in this study versus abyssal peridotite compositions from Day et al. 2017. Primitive mantle normalization given in McDonough and Sun (1995).

We analyzed three lavas from Aitutaki; nephelinite that hosts the xenoliths (c.f., Fodor et al., 1982), an ankaramite (picro-basalt), and an alkali basalt. The lavas range from 11.3 to 15.5 wt.% MgO with high $Al_2O_3$ (9.4-11.7 wt.%), CaO (10.2-13.4 wt.%), and $TiO_2$ (2-2.8 wt.%) and loss on ignition from 2.3 to 4.1 wt.%.

As expected for mantle residues after partial melt extraction, there are high concentrations of compatible elements in the low-Al xenoliths (177-3392 ppm Cr, 1106-2416 ppm Ni, 80-133 ppm Co) compared with the lavas (202-1150 ppm Cr, 167-565 ppm Ni, 63-70 ppm Co), with the high-Al xenoliths lying generally intermediate to these values (643-3544 ppm Cr, 231-997 ppm Ni, 44-

79 ppm Co). In an incompatible trace element plot *(Figure 7)*, low-Al xenoliths show depletions in K, Ti, Zr, and Hf, and relative enrichments in U (0.025 to 0.202 ppm), Pb (0.093 to 2.31 ppm), and Sr (12.6 to 78 ppm). The presence of U and Sr enrichment is similar to that in abyssal peridotites (Day et al., 2017), although the extent of enrichment in Aitutaki xenoliths is not as pronounced. Low-Al xenoliths AK-1005, AK-1006, and AK-1017 also have substantially elevated Cs. In general, abundances of the incompatible trace elements are <10 and >0.1 × PM values. In a rare earth element (REE) plot (***Figure 8***), low-Al xenoliths show a slight negative slope with most lherzolites showing slight light REE enrichments while the harzburgite and dunite are more depleted. Lanthanum/Yb ratios range from 2.3 to 29.2 with a standard deviation of 6.9.

High-Al xenoliths show slight depletions in Zr and Ti, and large depletions in K (8.30 to 1400 ppm) and P (74.2 to 148 ppm) (***Figure 9***). In general, abundances of the incompatible trace elements are <20 and >0.1 × PM values. A REE plot (***Figure 10***) shows a slight negative slope for high-Al xenoliths, with the high $Al_2O_3$ pyroxenite sample having a convex-upward pattern (Pr to Ho). Lanthanum/Yb ratios range from 5.01 to 9.4 with a standard deviation of 1.7. In ***Figure 9***, lavas show much greater enrichment in incompatible trace elements than the high-Al xenoliths but have similar primitive mantle-normalized patterns, suggesting evidence of melt-rock reaction between melts responsible for the lavas, and the xenoliths. However, anomalies in Zr (130.5 to 250 ppm) and Hf (3.5 to 5.6 ppm) for the lavas are not as pronounced in the xenoliths. ***Figure 10*** shows a steeper negative slope for the lavas than the high-Al xenoliths. Lanthanum/Yb ratios range from 14.3 to 60.7.
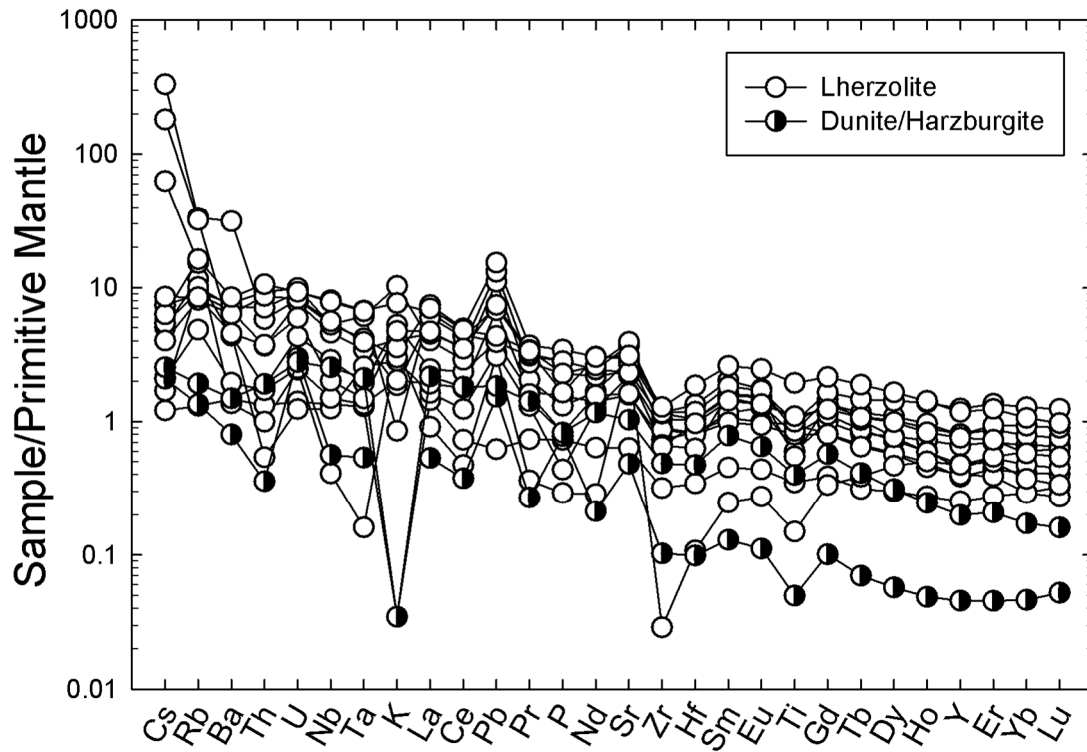
**Figure 7:** Primitive mantle normalized plot of Aitutaki 'Low-Al' (lherzolite, harzburgite and dunite) xenoliths. Primitive mantle normalization given in McDonough and Sun (1995).
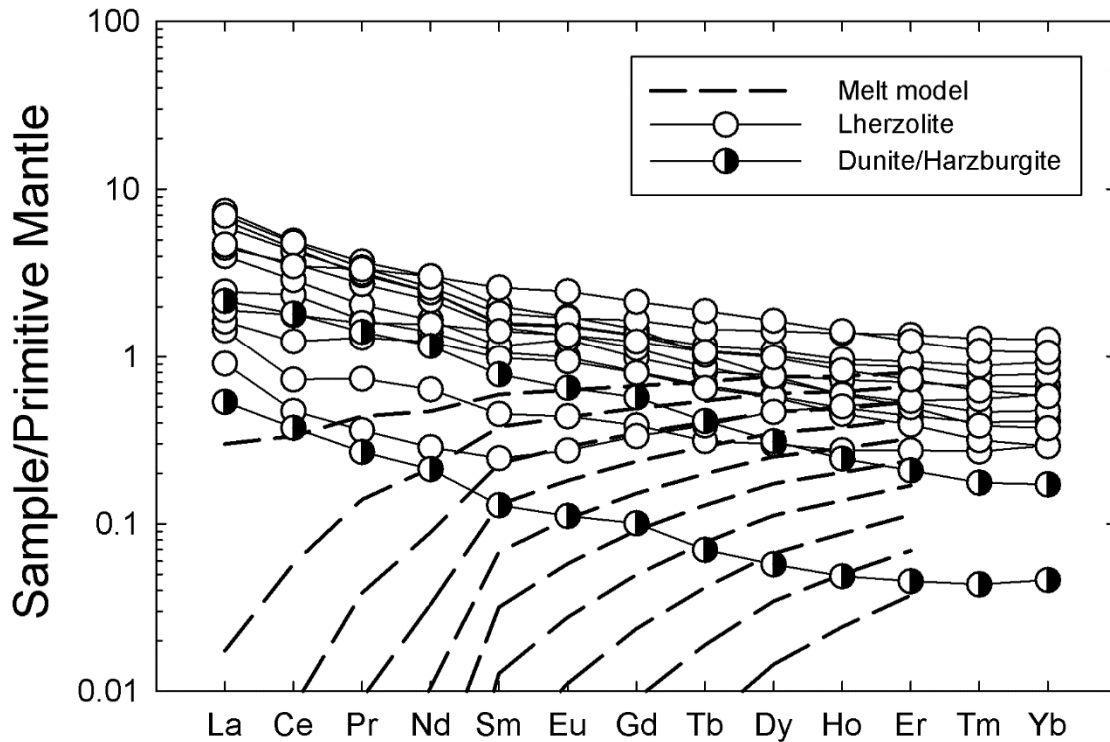
**Figure 8:** Primitive mantle normalized plot of Aitutaki 'Low-Al' (lherzolite, harzburgite and dunite) xenoliths. Primitive mantle normalization given in McDonough and Sun (1995). Black dashed lines indicate 2% melt increments for a non-modal fractional melting model, where increasing melt depletion results in lower absolute abundances of the REE and increasing depletion in the LREE relative to HREE. As a robust means for estimating melt depletion, we use a non-modal fractional melting model for whole-rock abyssal peridotites that assumes an initial starting composition of depleted MORB mantle (Workman & Hart, 2005), uses partition coefficients from Suhr et al. (1998) for spinel and Sun & Liang (2014) for olivine and pyroxene, and melt reactions discussed in Warren (2016). The model leads to general levels of melt depletion similar to those calculated using the spinel compositions. Model parameters and normalization are from Day et al. (2017).
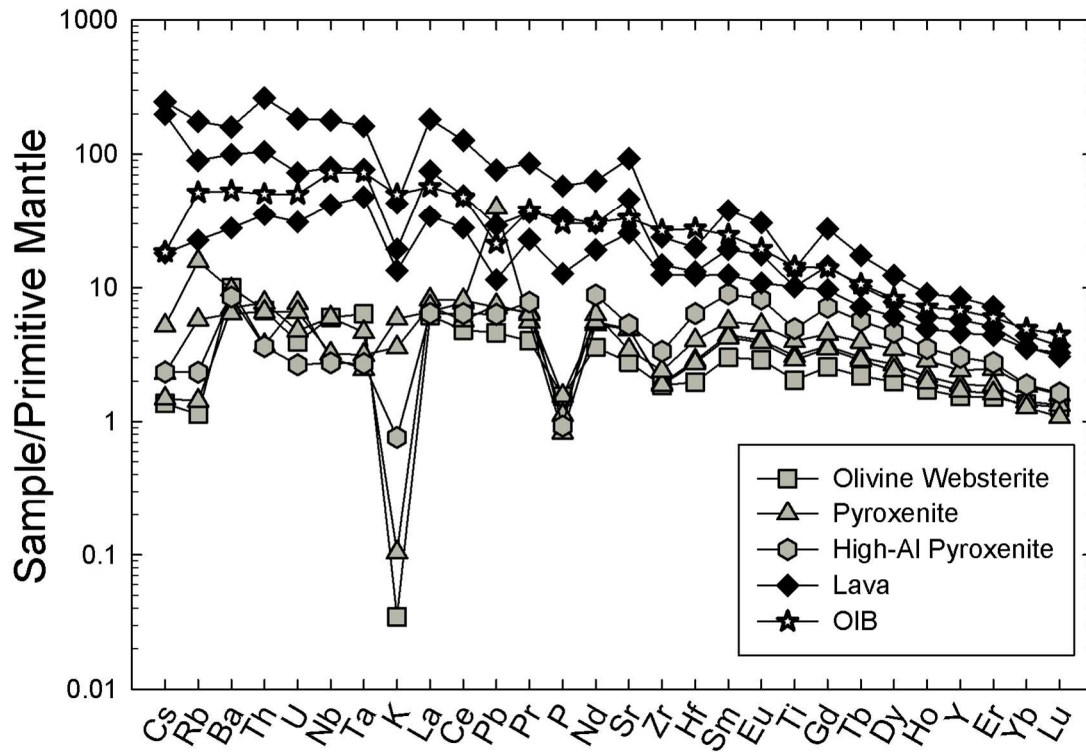
**Figure 9:** Primitive mantle normalized plot of Aitutaki 'High-Al' (olivine websterite, pyroxenite, and high-Al pyroxenite) xenoliths and lavas measured in this study. Ocean Island Basalt (OIB) from McDonough and Sun (1989). Primitive mantle normalization from McDonough and Sun (1995).
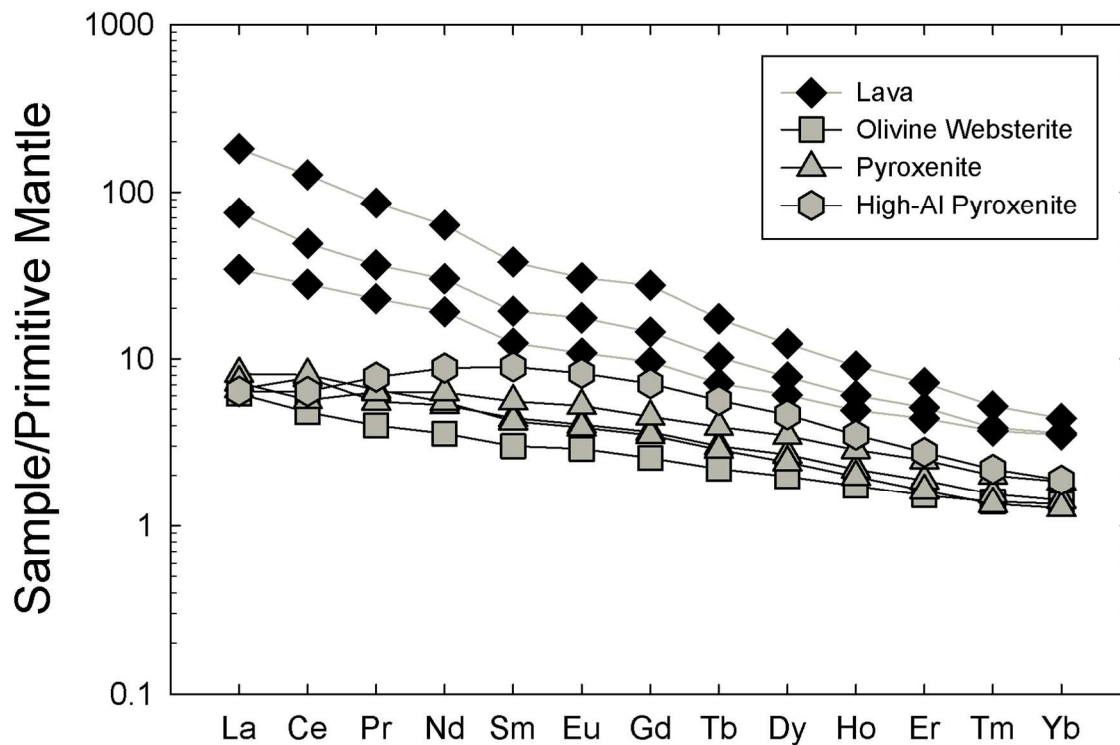
**Figure 10:** Primitive mantle normalized plot of Aitutaki 'High-Al' (olivine websterite, pyroxenite, and high-Al pyroxenite) xenoliths and lavas measured in this study. Primitive mantle normalization from McDonough and Sun (1995).

## 3.3. Highly siderophile element (HSE) abundances and osmium isotope systematics

In this study, due to limited samples mass, samples were generally measured once, except for samples AK-1021 and AK-1028 that were both measured twice, using different fragments of the xenoliths that were crushed and powdered separately to determine the possibility of cm-scale heterogeneities within each sample, and are referred to as AK-1021-A, AK-1021-B, AK-1028-A, and AK-1028-B.

The highly siderophile element (HSE: Os, Ir, Ru, Pt, Pd, Re) concentrations of one dunite, one harzburgite, 10 lherzolites, two pyroxenites, a high-$Al_2O_3$ pyroxenite, and two olivine websterites,

as well as two lavas (an ankaramite and nephelinite), are reported in *Table 2*. In general, low-Al xenolith samples have fairly-flat primitive mantle (PM) normalized HSE patterns ranging between ~0.1 to 1 times PM values with Os ranging from 0.531 to 4.26 ppb (*Figure 11*). Samples AK-1021-A and AK-1021-B, taken from a single xenolith, represent the most enriched and depleted samples for Re (0.011 to 0.57 ppb), and are also most depleted in Pd (0.8 to 0.94 ppb) compared to the range of other lherzolite samples (2.35 to 4.56 ppb). Palladium/Ir ratios range from 0.54 to 3.05 with a standard deviation of 0.69, while Ru/Ir ratios range from 1.72 to 2.40 with a standard deviation of 0.19.
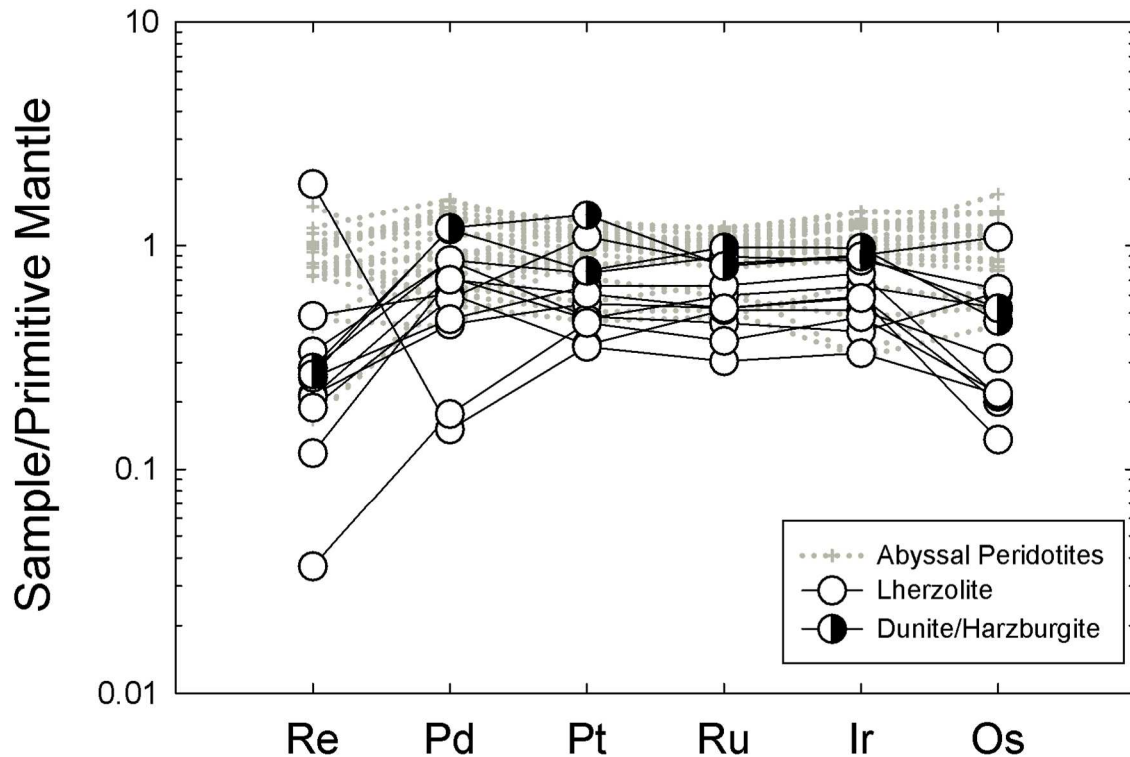


**Figure 11:** Primitive mantle normalized plot of Aitutaki 'Low-Al' (lherzolite, harzburgite and dunite) xenoliths versus abyssal peridotite compsitions from Day et al., 2017, Liu et al., 2008 and 2009, and Stracke et al. 2011. Data are shown with most incompatible elements on the left (cf. Day, 2013). Primitive mantle normalization given in McDonough and Sun (1995).

The high- and low-Al xenoliths and lava concentrations are reported in *Table 2*. The lherzolites, harzburgite, and dunite are mostly clustered in *Figure 12* with an average $^{187}Os/^{188}Os$ of 0.1264 ±

0.0043 (1 SD; n = 12) and a median value of 0.1279. All of these peridotites have low $^{187}Re/^{188}Os$ values ranging from 0.062 to 3.25. Notably, the splits AK-1021-A and AK-1021-B have similar $^{187}Os/^{188}Os$ values but AK-1021-A has significantly higher $^{187}Re/^{188}Os$ values indicating that there is heterogeneity at the cm scale for Re in this sample.



**Figure 12:** $^{187}Re/^{188}Os$-$^{187}Os/^{188}Os$ diagram for Aitutaki 'Low-Al' and 'High-Al' xenoliths and lavas measured in this study. Figure also shows 0 Ma and 100 Ma reference isochrons assuming mantle Os isotope evolution.

The remaining high-Al xenoliths and the lavas are shown in ***Figure 13***. Olivine websterite samples have broadly similar HSE abundances to the lherzolites, whereas the pyroxenite and high $Al_2O_3$ pyroxenite samples have steep HSE patterns with pronounced relative depletions in Ru, Ir and Os relative to Pt and Pd, and in this respect are similar to the lavas. The high-Al xenoliths exhibit variable concentrations in Os (0.049 to 1.11 ppb), Ir (0.039 to 2.66 ppb), Ru (0.196 to 5.48

ppb), Pt (0.238 to 5.55 ppb), Pd (0.692 to 4.83 ppb), and Re (0.040 to 0.264 ppb). Palladium/Ir ratios range from 0.948 to 42.1 with a large standard deviation (17.8), while Ru/Ir ratios range from 1.61 to 4.98 with a smaller standard deviation (1.37). Lava samples have similar primitive mantle normalized patterns, with the exception of Pt and Ir, both of which are more depleted in the nephelinite sample.

The high-Al xenoliths show much more variable concentrations in both $^{187}Os/^{188}Os$ (0.1263 to 0.1469) and $^{187}Re/^{188}Os$ (0.173 to 11.0) than the low-Al xenoliths. The two pyroxenite samples, AK-1023-2 and AK-1023-3, and lavas, AK-1017-L and AK-1025-L, show similar $^{187}Os/^{188}Os$ values but significantly different $^{187}Re/^{188}Os$ values. However, the two olivine websterite samples, AK-1028-A and AK-1028-B, have similar $^{187}Re/^{188}Os$ values but AK-1028-B has higher $^{187}Os/^{188}Os$ values.

Standard reference material, harzburgite MUH-1 (aliquots red, blue and black, from T. Meisel, University of Leoben, Austria) was also analyzed in this study and values for it are reported in *Table 2*. The average Re is 0.24 ± 0.12 with a median value of 0.21, Pd is 10.3 ± 2.1 with a median value of 10.1, Pt is 8.09 ± 2.69 with a median value of 7.73, Ru is 8.15 ± 2.5 with a median value of 7.9, Ir is 3.99 ± 1.42 with a median value of 3.73, and Os is 4.27 ± 1.76 with a median value of 4.14 (2SD; n = 4). The average $^{187}Os/^{188}Os$ values for the standard are 0.1260 ± 0.0017 with a median value of 0.126; the average $^{187}Re/^{188}Os$ values is 0.228 ± 0.093 with a median value of 0.221 (2SD; n = 4).
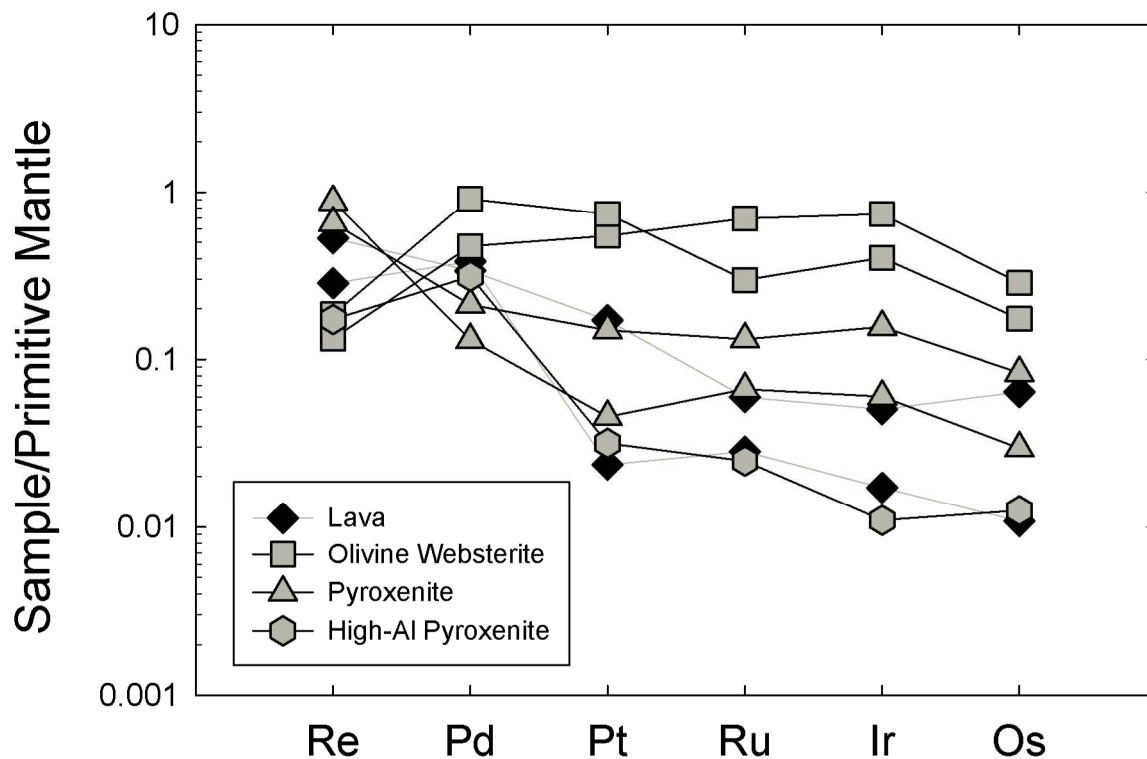
**Figure 13:** Primitive mantle normalized highly siderophile element patterns for Aitutaki 'High-Al' (olivine websterite, pyroxenite, and high-Al pyroxenite) xenoliths and lavas measured in this study. Data are shown with most incompatible elements on the left (cf. Day, 2013). Primitive mantle normalization given in McDonough and Sun (1995).

## 4. Discussion

## 4.1. Aitutaki lavas formed by low-degree melting of an enriched OIB source

Aitutaki is part of the Cook Islands and the westernmost of the exposed volcanoes of the Cook-Austral hotspot track (e.g., Clouard & Gerbault, 2008). The hotspot responsible for Aitutaki is considered to be presently underlying the Macdonald seamount (Morgan et al., 1972), located greater than 2200 km southeast of Aitutaki (Bonneville et al. 2006). Using K-Ar age dating techniques, Aitutaki's major volcanic rock types, olivine nephelinite and basanite (Wood, 1967; Wood, 1978a), span a range from $0.66 \pm 0.06$ Ma (Dalrymple et al. 1975) to $8.05 \pm 0.66$ Ma

(Turner et al., 1981), while the lithosphere beneath Aitutaki has been found to be ~87 Ma (Calmant et al., 1990).

We show that our lavas, found in the northwest end of the tuff ring on the main islet of Aitutaki (*Figure 1*), represent low degree (< 1%) partial melts of an enriched mantle source (*Figure 14*), and consider this to be due to rejuvenated volcanism induced by lithospheric flexure from loading of the local plate by Rarotonga which has an age of $1.19 \pm 0.04$ Ma to $1.83 \pm 0.13$ Ma (Dalrymple et al. 1975). Comparison of incompatible trace-element (ITE) abundances for the three Aitutaki lavas show that they are similar to one another (*Figure 9*). It has previously been shown that Aitutaki lavas have EM1/EM2-type signatures, reflected by their ranges in $^{87}Sr/^{86}Sr$ (0.70440 to 0.70506) and $^{143}Nd/^{144}Nd$ (0.512715 to 0.512789) (Schiano et al., 2001; Nakamura and Tatsumoto., 1988). A comparison of the HSE patterns for the nephelinite and ankaramite with Hawaiian (Ireland et al. 2009) and Canary Island lavas (Day et al. 2010) show that Aitutaki lavas have steeper HSE patterns than Hawaii and compare well with Canary Island alkali basalt lavas, except for greater depletion in Re and Pt in Aitutaki lavas compared to Canary island lavas. Aitutaki lavas also have slightly radiogenic $^{187}Os/^{188}Os$ signatures (*Figure 12*), with an average ratio of 0.1363, similar to that previously measured for an Aitutaki lava of 0.1370 (Schiano et al., 2001). Enriched major- and trace-element compositions, compared with the depleted xenoliths that the lavas entrain, radiogenic osmium values and steep HSE patterns are all consistent with Aitutaki lavas originating from an enriched mantle source.
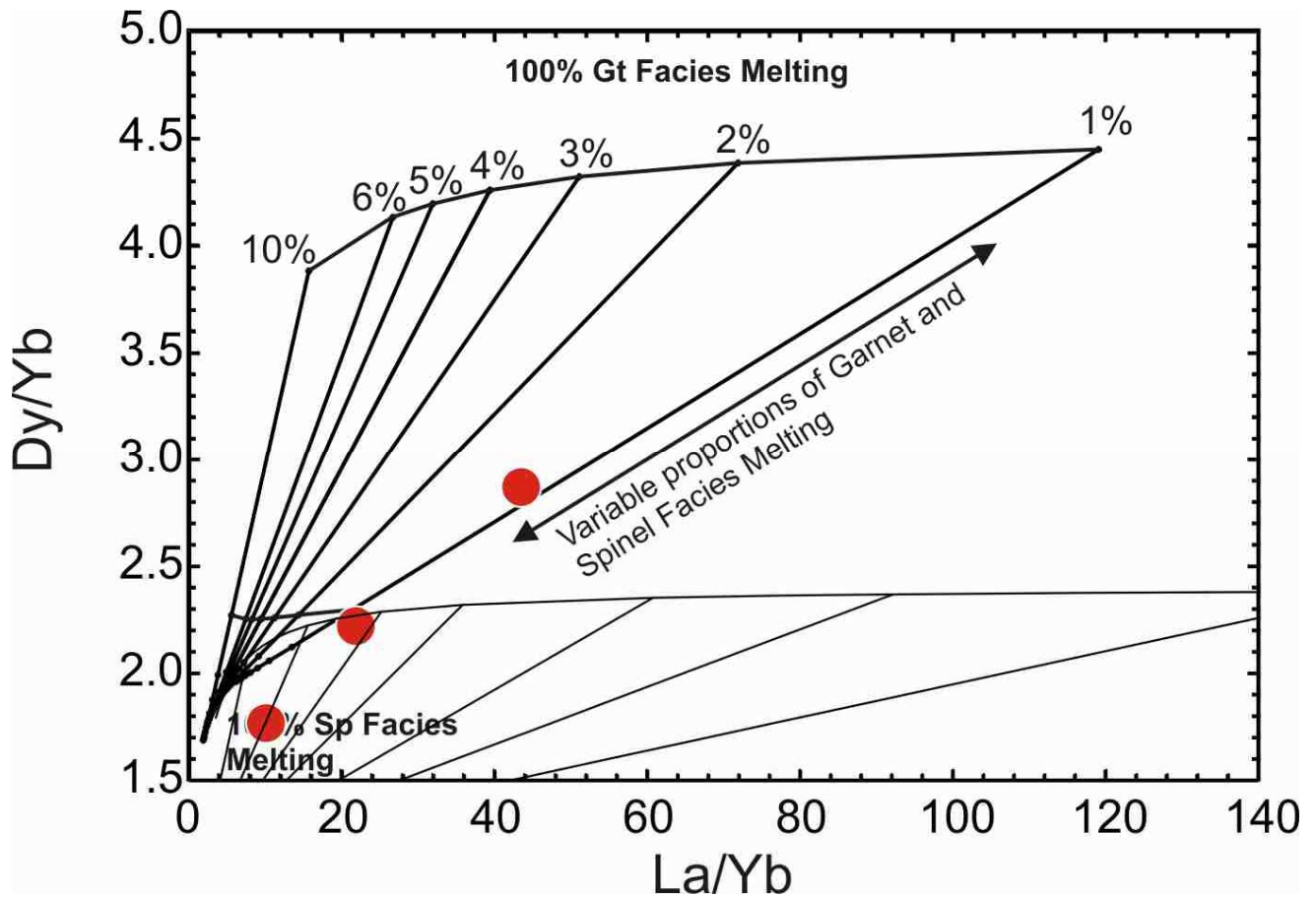
**Figure 14:** La/Yb versus Dy/Yb for Aitutaki lavas (red circles). Shown are models of melt compositions produced by 1-20% of incremental batch partial melting of a primitive mantle source, with 0-100% melting occurring in the presence of residual garnet (Sp100, Gar100) (thick bold lines) and for a MORB-like partial melt model (fine lines). The melting models assume the following modes and proportions of olivine, orthopyroxene, clinopyroxene and spinel/garnet, respectively: 0.4/0.3/0.1/0.1 and 0.25/0.25/0.25/0.25. Primitive mantle normalization and MORB data are from Sun and McDonough (1989).

## 4.2. Alteration in the Aitutaki xenolith suite

Hand samples of high- and low-Al xenoliths show variable evidence for alteration. Some xenoliths appear fresh while others have distinct reddish alteration patches from weathering of olivine. The loss on ignition (LOI) content for both xenolith suites ranges between 0.3 to 4 wt. %. These low LOI values and petrography of the samples support observations that post-eruptive alteration is limited. Uranium, Sr, and Pb - three elements that have been suggested to reflect alteration during serpentinization (e.g., Niu 2004; Deschamps et al., 2011) have been plotted against LOI (*Figure 15* and *Figure 16*) and we see little to no correlation for Pb and U. However,

Sr shows a slight positive correlation suggesting potential evidence for post-eruptive alteration for the more fluid mobile elements.
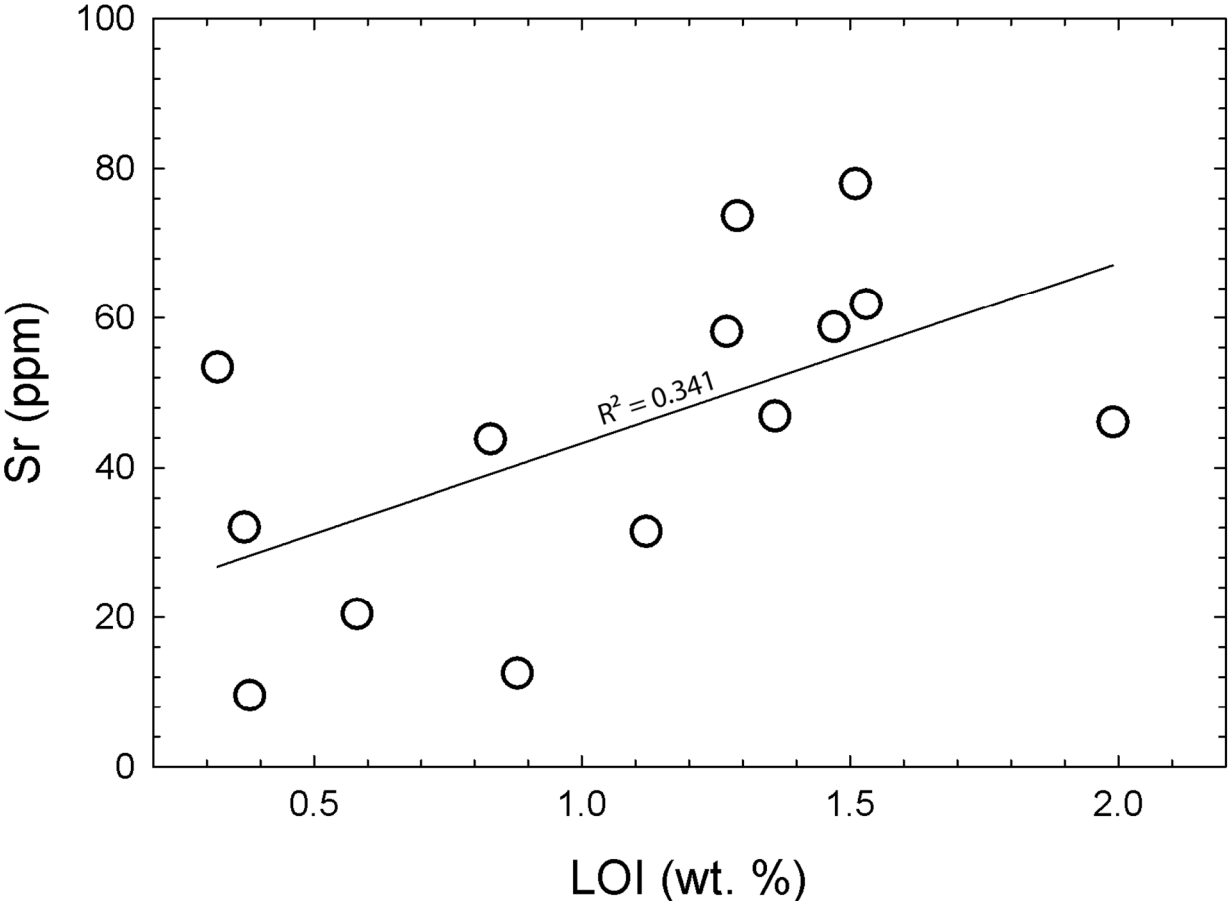


**Figure 15:** LOI (wt. %) versus Sr for 'Low-Al' and 'High-Al' xenoliths measured in this study.
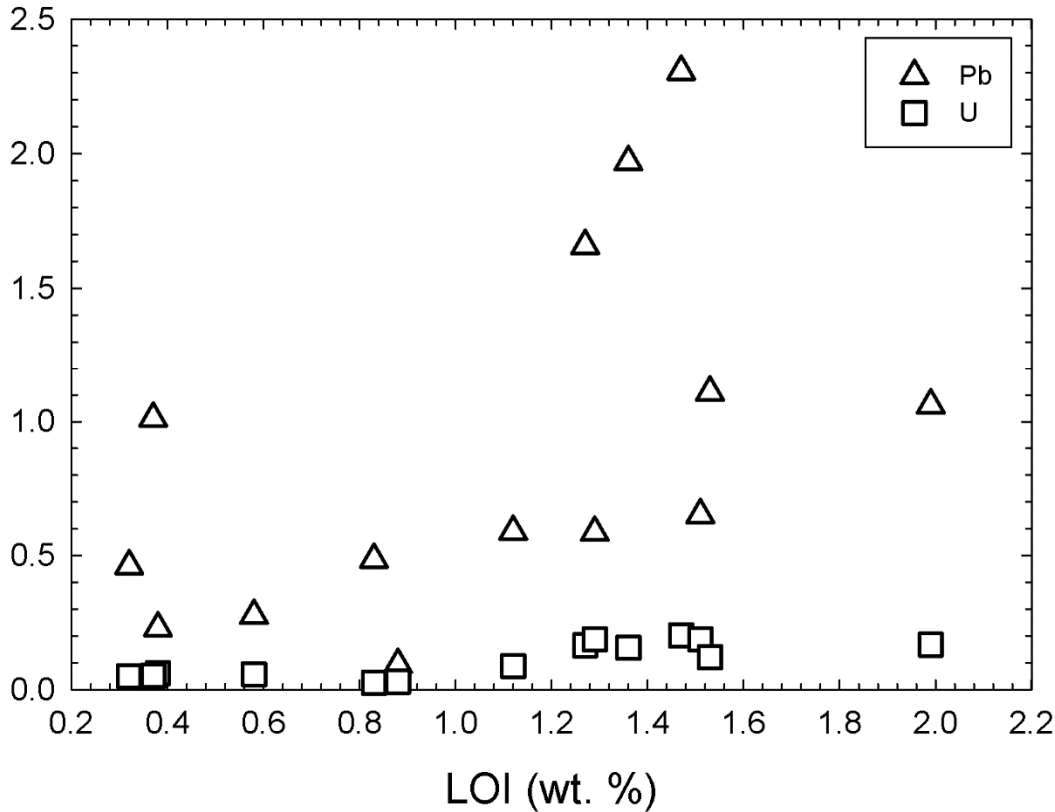
**Figure 16:** LOI (wt. %) versus Pb and U for 'Low-Al' and 'High-Al' xenoliths measured in this study.

## 4.3. Melt rock reaction in the Aitutaki xenolith suite

Aitutaki lavas and high-Al xenoliths both show slight depletions in Zr and Hf, a large depletion in P, and high variability in K on an ITE plot (*Figure 9*). High-Al xenoliths also exhibit elevated REE abundances (*Figure 9* and *10*), and in an MgO versus $Al_2O_3$ plot (*Figure 5*) span the range between Aitutaki lavas and abyssal peridotites. These lines of evidence all suggest that melt-rock reaction is responsible for the formation of the high-Al xenoliths by melt infiltration of Aitutaki lava parental melt like compositions. Melt-rock reaction is supported by HSE patterns (*Figure 13*) for the pyroxenite and high $Al_2O_3$ pyroxenite samples that are similar to the lava compositions, yet HSE patterns for the olivine websterites are similar to the low-Al xenoliths.

In general, low-Al xenoliths also exhibit evidence for melt-rock reaction, including LREE inflections similar to the lavas (*Figure 7*). Elements Ti, K, Zr, and Hf all show similar depletions

to the lavas, while samples AK-1005, AK-1006, and AK-1017 all have elevated Cs and Rb, much like the host nephelinite. However, the LREE in low-Al xenoliths (*Figure 7* and *8*) are more depleted and have a steeper negative slope than the lavas or high-Al xenoliths. Low-Al xenoliths generally cluster to low $Al_2O_3$ and high MgO contents, like abyssal peridotites (*Figure 5*). HSE patterns for low-Al xenoliths are much flatter than the lavas, with elevated Os, Ir and Ru abundances (*Figure 11*) and, notably, the patterns for the olivine websterite samples are more similar to the low-Al xenoliths than to the lavas or high-Al xenoliths (*Figure 13*), suggesting a threshold for melt-rock reaction to strongly affect the HSE.

Selected hand specimens are shown in *Figure 3*. Harzburgite and dunite samples are not shown due to limited available sample mass. In the figure, the lherzolite is shown with patchy red olivine alterations and dark clinopyroxene. In general, the lherzolite is fairly fresh in comparison to the two pyroxenite samples where the red patchy alterations are much more prevalent and clinopyroxene is much more abundant. The olivine websterite sample is similar to the pyroxene samples with regards to alteration but it lacks the abundant clinopyroxenes. These lines of evidence support the geochemical indices of melt-rock reaction recognized in the Aitutaki xenolith suite.

Since Aitutaki's lithosphere is over 80 Ma we can assume that the island sits atop 80 to 90 km thick lithosphere (e.g., Sclater et al., 1970). With limited evidence of post-eruptive alteration to the xenolith suite, along with the evidence presented above for melt-rock reaction, and that our samples are all spinel-bearing, we suggest that the xenoliths originate from Pacific plate oceanic lithosphere. Contrastingly, the lavas come from a distinct and enriched mantle source. Our results imply that the lavas originated at a depth greater than or equal to 90 km, implying they started in the asthenosphere, or the asthenosphere/lithosphere boundary, and entrained the xenoliths on their way to the surface.

## 4.4. Heterogeneity within the lithosphere of Aitutaki

It has been recognized that mantle heterogeneity exists in Earth on scales ranging from hundreds of kilometers to meters (e.g., Zindler and Hart, 1986; Hart 1984; Hofmann, 1997, 2003; Hart and Hauri, 1992), but at the scale of the hand specimen, heterogeneity is less well documented. In

order to investigate this issue, we measured four aliquots of MUH-1 and split hand samples AK-1021 and AK-1028 into four separately analyzed fragments, each with their own individual crush and powder. Harzburgites are notoriously more heterogenous than lherzolites for refractory trace elements, such as the HSE (e.g., Luguet & Reisberg, 2016), due to the presence of micro-inclusions of HSE-rich sulfides and alloys. Therefore, the standard reference material MUH-1 represents a threshold for the heterogeneity we might expect from the 'nugget effect' within sample powders. MUH-1 shows a maximum variation of twenty percent with respect to absolute concentrations of the HSE, while the variations found within the Aitutaki xenoliths are greater than one hundred percent. While there is no doubt that nuggeting can generate some of the abundance variations observed in Aitutaki xenoliths, this effect alone, cannot account for the entire range of HSE abundances in the samples.

Within the Aitutaki xenolith suite itself, centimeter-scale heterogeneity is apparent in the case of samples AK-1021-A/B and AK-1028-A/B (*Figure 12*). Sample AK-1021-A has significantly higher $^{187}Re/^{188}Os$ than AK-1021-B but both are similar with respect to $^{187}Os/^{188}Os$, reflecting late $^{187}Re$ addition via melt re-fertilization to AK-1021-A. Contrastingly, sample AK-1028-B has significantly higher $^{187}Os/^{188}Os$ than AK-1028-A but both are similar with respect to $^{187}Re/^{188}Os$. We interpret the higher $^{187}Os/^{188}Os$ in AK-1028-B to reflect greater addition of radiogenic $^{187}Os$ from infiltrating melt similar to the host nephelinite, consistent with variations seen in sample clinopyroxene abundances in the websterite xenoliths. Both of these small-scale heterogeneities support a model of cm-scale heterogeneity of melt infiltration within the mantle beneath Aitutaki. Heterogeneity undoubtedly exists for HSE abundances and $^{187}Os/^{188}Os$ in the suite of rocks that we have analyzed, and the cause of this heterogeneity is a mixture of nugget effect (~20% variation) and heterogeneity, melt infiltration processes and prior melt-depletion (~50-80% of the total variation).

## 4.5. Are lherzolites primary or melt infiltrated?

Aitutaki lherzolites represent oceanic lithosphere and generally compare well to abyssal peridotites, which represent oceanic mantle that has been processed through ridges (Niu et al.,

2004; Day et al., 2017).  Evidence for similarities with abyssal peridotites are shown from similar major element compositions, high concentrations of compatible elements, and very similar HSE patterns in *Figures 5, 7, and 11*.  However, as I have demonstrated, Aitutaki lherzolites show evidence for melt infiltration by enriched OIB-type melts.  It is visible in hand sample that lherzolites have clinopyroxene added back into the rock through melt infiltration processes (*Figure 3*), suggesting that lherzolites may have started off as harzburgite, or even dunite. Additionally, light rare earth element and incompatible trace element abundances for the lherzolites are inconsistent with evidence for significant melt depletion (*Figure 7* and *8*). Finally, olivine compositions (*Figure 4*) track progressive Fe-enrichment from the olivine websterites through to the lherzolites and harzburgites, that is similarly tracked by enriched $^{187}Os/^{188}Os$ in more melt-refertilized xenoliths. All of these lines of evidence cast doubt on the Aitutaki xenoliths representing primary mantle compositions.

  The overarching evidence is that melts with compositions similar to lavas have pervasively melt-refertilized the oceanic lithosphere beneath Aitutaki subsequent to formation of the oceanic lithosphere at the mid-ocean ridge.  I suggest that melt-rock reaction has driven compositions from dunite/harzburgite to lherzolite and even olivine websterite and pyroxenite due to pervasive but heterogeneous melt-rock reaction (*Figure 17*). In this model, small degrees of melt from the asthenosphere and/or lithosphere/asthenosphere boundary make their way towards Earth's surface through 80 to 90 km of lithosphere, primarily consisting of harzburgite but also containing old mantle domains consisting of dunite/harzburgite.  Proximity to melt veins and melt conduits may reflect and bias the rock types that ultimately get expressed at the surface.  The rocks nearest the melt veins would see the greatest melt-rock reaction, driving the compositions to pyroxenite and olivine websterite.  Further from these regions of pervasive melt-rock reaction more cryptic metasomatism would drive compositions from harzburgite to lherzolite.  The expression of dunite/harzburgite at the surface reflects the least amount of melt-rock reaction.  Overall, the observations are that Aitutaki lherzolites started as lithologies more like harzburgite or dunite and through re-fertilization of the mantle via hotspot lavas, were transformed by melt infiltration.
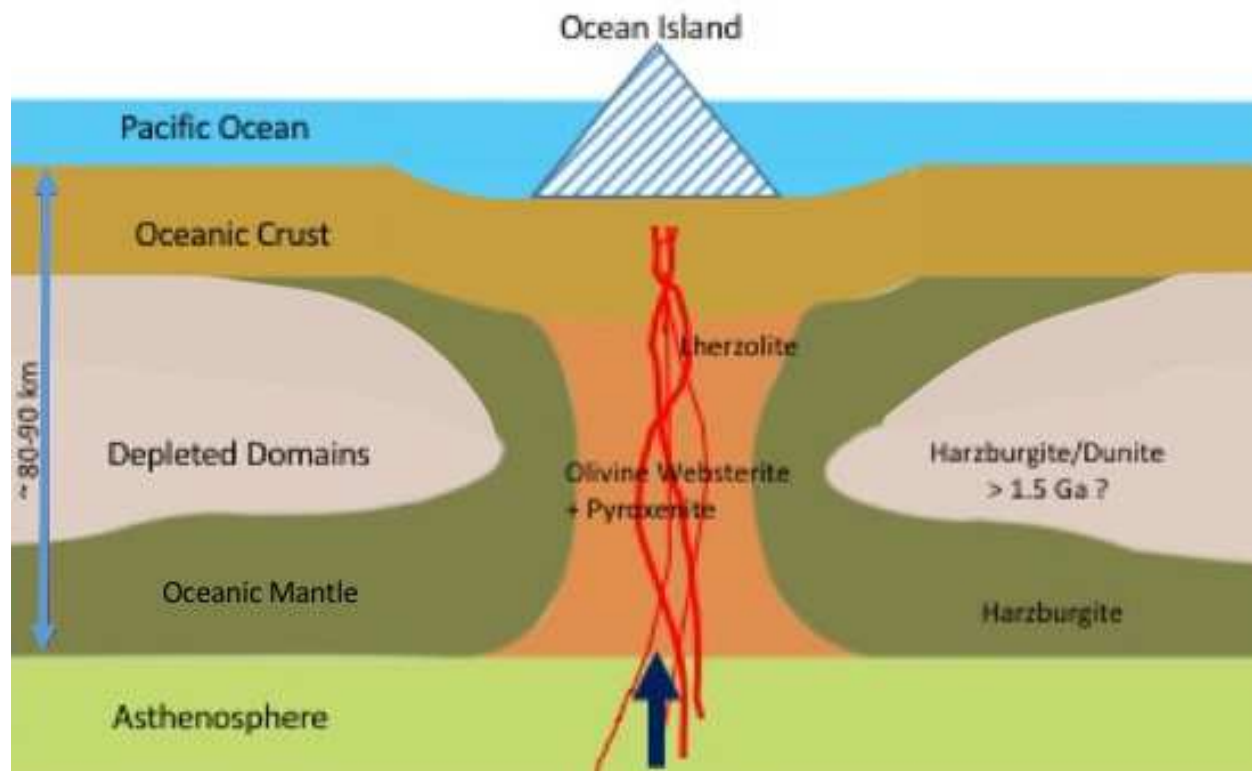
**Figure 17:** Summary diagram of melt infiltration beneath Aitutaki and of the possible relationship of Western Pacific mantle lithosphere.

## 4.6. Implications for the nature of the Western Pacific Lithosphere

Depleted mantle domains have been found in Hawaii (e.g., Simon & Neumann, 2008), Samoa (Jackson et al., 2016), and now the Cook Islands (this study), all of which are found in the Western Pacific. Aitutaki xenoliths have preserved old melt depletion ages up to 1.5 Ga, and Jackson et al. (2016) have reported old melt depletion ages in Savai'i up to 1.5 Ga and in Tubuai up to 1.8 Ga, both of which are part of the Samoan Island chain (*Figure 18*). However, most of the studied peridotites in these locations trend to much younger depletion ages.
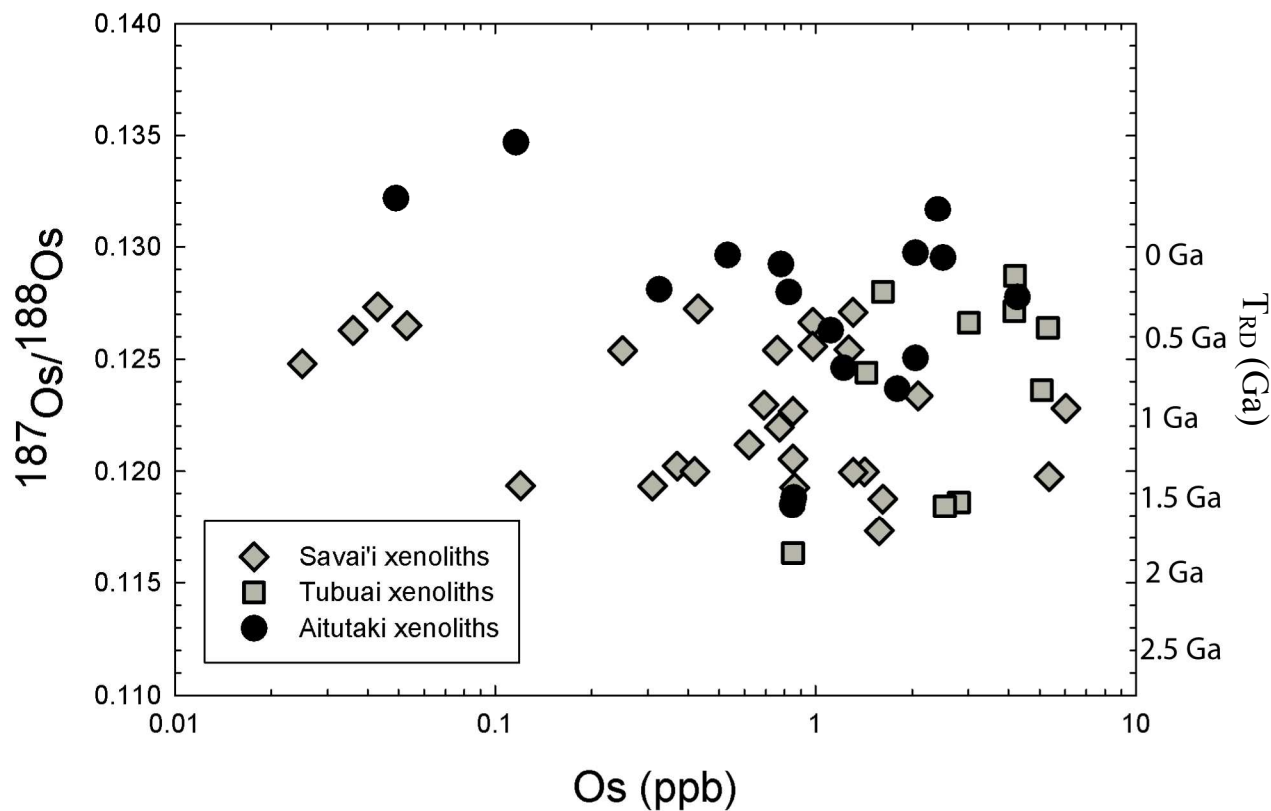
**Figure 18:** Relationship between $^{187}Os/^{188}Os$ and Os concentrations for Aitutaki xenoliths. Savai'i and Tubuai xenoliths (Jackson et al., 2016) are also plotted for comparison.

New results of detailed trace-element geochemistry and HSE abundances allow us to identify melt-refertilization as an important process in the generation of the Aitutaki xenolith suite. Extrapolation of this information to Savaii and Tubuai xenoliths leads to the inference that the variations in Os isotope compositions seen throughout these regions reflects later melt-infiltration processes superimposed on prior melt depletion. The western pacific lithosphere appears similar to oceanic mantle preserved by abyssal peridotites (e.g., Lassiter et al., 2014), but that it can trend to much old depletion ages. On top of this, while melt depletion for the lherzolites and harzburgites are typical for abyssal peridotite (~10 to 14 %; *Figure 8*), the single Aitutaki dunite xenolith preserves evidence for extreme melt depletion, up to 20 % (AK 1008). Large regions of the Western Pacific mantle lithosphere may represent strongly depleted mantle that was subjected to

Mesoproterozoic melt depletion, but melt-refertilization processes are pervasive in ocean island xenolith suites and bias determination of the extent of lithospheric melt-depletion.

# 5. Conclusions

Aitutaki xenoliths represent oceanic lithosphere that has been entrained by low-degree partial melts from an enriched mantle source. It has been shown that limited and variable evidence for post-eruptive alteration to Aitutaki xenoliths exists in this suite of rocks, however, strong evidence exists for pervasive melt-rock reaction to both high- and low-Al xenoliths. The presence of abundant lherzolites in our suite of Aitutaki xenoliths shows that melt infiltration via hotspot magmas can fundamentally modify oceanic lithosphere and more generally, melt-refirtilization by OIB melts can strongly bias evidence from OIB derived mantle peridotites.

Compositions of OIB xenoliths, including Aitutaki, would lead to the conclusion of the existence of a fertile mantle, yet the Pacific plate is more-likely significantly melt depleted. Evidence for old time of rhenium depletion ages up to 1.5 Ga, along with some samples that show extensive melt depletion, up to 20 % (*Figure 8*), indicate that Western Pacific lithosphere could be highly depleted and may have experienced a Mesoproterozoic melt depletion event that has been recorded in Savai'i, Tubuai, and Aitutaki.

# Future Work

There are three areas of future work that are likely to be beneficial in the study of Aitutaki xenoliths and the Western Pacific oceanic mantle lithosphere:

First, polished thin-sections are being prepared in order to do more detailed petrology and petrography and to confirm melt refertilization and melt-extraction processes. The lack of available polished thin-sections for this project was due, in part, to the limited available material, but would definitively confirm the relationship of melt refertilization seen in the major- and trace-element data and the relationship inferred in *Figure 17*.

Second, further study of Samoan xenoliths from Savai'i and Tubuai for trace-element compositions, highly siderophile element abundances and other compositional information would enable assessment of melt-refertilization processes as shown for Aitutaki.

Third, hafnium isotope compositions would be valuable for gaining a more complete view of melt depletion in Aitutaki. Evidence for Hf isotopes being a long-term recorder of melt-depletion in abyssal peridotites (Stracke et al., 2011), has been recently questioned based on coupled Os-Hf isotope systematics in abyssal peridotites (Day et al., 2017), and Western Pacific mantle lithosphere samples would be useful for investigating melt-depletion relationships in lithophile and chalcophile isotope systems.

# References:

Afonso, J.C., Ranalli, G. and Fernandez, M., 2007. Density structure and buoyancy of the oceanic lithosphere revisited. *Geophysical Research Letters*, *34*(10).

Birck, J.L., Barman, M.R. and Capmas, F., 1997. Re-Os isotopic measurements at the femtomole level in natural samples. *Geostandards and Geoanalytical Research*, *21*(1), pp.19-27.

Bonneville, A., Dosso, L. and Hildenbrand, A., 2006. Temporal evolution and geochemical variability of the South Pacific superplume activity. *Earth and Planetary Science Letters*, *244*(1), pp.251-269.

Boyd, F.R. and Mertzman, S.A., 1987. Composition and structure of the Kaapvaal lithosphere, southern Africa. *Magmatic processes: physicochemical principles*, *1*, pp.3-12.

Calmant, S., Francheteau, J. and Cazenave, A., 1990. Elastic layer thickening with age of the oceanic lithosphere: a tool for prediction of the age of volcanoes or oceanic crust. *Geophysical Journal International*, *100*(1), pp.59-67.

Clouard, V. and Gerbault, M., 2008. Break-up spots: Could the Pacific open as a consequence of plate kinematics? *Earth and Planetary Science Letters*, *265*(1-2), pp.195-208.

Cohen, A.S. and Waters, F.G., 1996. Separation of osmium from geological materials by solvent extraction for analysis by thermal ionisation mass spectrometry. *Analytica Chimica Acta*, *332*(2-3), pp.269-275.

Dalrymple, G.B., Jarrard, R.D. and Clague, D.A., 1975. K-Ar ages of some volcanic rocks from the Cook and Austral Islands. *Geological Society of America Bulletin*, *86*(10), pp.1463-1467.

Day, J.M.D., Peters, B.J. and Janney, P.E., 2014. Oxygen isotope systematics of South African olivine melilitites and implications for HIMU mantle reservoirs. *Lithos*, *202*, pp.76-84.

Day, J.M.D., Waters, C.L., Schaefer, B.F., Walker, R.J. and Turner, S., 2016. Use of Hydrofluoric Acid Desilicification in the Determination of Highly Siderophile Element Abundances and Re-Pt-Os Isotope Systematics in Mafic-Ultramafic Rocks. *Geostandards and Geoanalytical Research*, *40*(1), pp.49-65.

Day, J.M.D., 2013. Hotspot volcanism and highly siderophile elements. *Chemical Geology*, *341*, pp.50-74.

Day, J.M.D., Walker, R.J. and Warren, J.M., 2017. 186 Os–187 Os and highly siderophile element abundance systematics of the mantle revealed by abyssal peridotites and Os-rich alloys. *Geochimica et Cosmochimica Acta*, *200*, pp.232-254.

Day, J.M.D., Pearson, D.G., Macpherson, C.G., Lowry, D. and Carracedo, J.C., 2010. Evidence for distinct proportions of subducted oceanic crust and lithosphere in HIMU-type mantle

beneath El Hierro and La Palma, Canary Islands. *Geochimica et Cosmochimica Acta*, *74*(22), pp.6565-6589.

Deschamps, F., Guillot, S., Godard, M., Andreani, M. and Hattori, K., 2011. Serpentinites act as sponges for fluid-mobile elements in abyssal and subduction zone environments. *Terra Nova*, *23*(3), pp.171-178.

Fodor, R.V., Bauer, G.R. and Keil, K., 1982. Ultramafic inclusions and megacrysts in olivine nephelinite, Aitutaki Island, Cook Islands. *New Zealand Journal of Geology and Geophysics*, *25*(1), pp.67-76.

Hart, S.R., 1984. A large-scale isotope anomaly in the Southern Hemisphere mantle. *Nature*, *309*(5971), p.753.

Hart, S.R., Hauri, E.H., Oschmann, L.A. and Whitehead, J.A., 1992. Mantle plumes and entrainment: isotopic evidence. *Science*, *256*(5056), pp.517-520.

Hirth, G. and Kohlstedt, D.L., 1996. Water in the oceanic upper mantle: implications for rheology, melt extraction and the evolution of the lithosphere. *Earth and Planetary Science Letters*, *144*(1-2), pp.93-108.

Hofmann, A.W., 1997. Mantle geochemistry: the message from oceanic volcanism. *Nature*, *385*(6613), p.219.

Ireland, T.J., Walker, R.J. and Garcia, M.O., 2009. Highly siderophile element and 187 Os isotope systematics of Hawaiian picrites: implications for parental melt composition and source heterogeneity. *Chemical Geology*, *260*(1), pp.112-128.

Jackson, M.G., Shirey, S.B., Hauri, E.H., Kurz, M.D. and Rizo, H., 2016. Peridotite xenoliths from the Polynesian Austral and Samoa hotspots: Implications for the destruction of ancient 187 Os and 142 Nd isotopic domains and the preservation of Hadean 129 Xe in the modern convecting mantle. *Geochimica et Cosmochimica Acta*, *185*, pp.21-43.

Johnson, K., Dick, H.J. and Shimizu, N., 1990. Melting in the oceanic upper mantle: an ion microprobe study of diopsides in abyssal peridotites. *Journal of Geophysical Research: Solid Earth*, *95*(B3), pp.2661-2678.

Kelemen, P.B., Dick, H.J. and Quick, J.E., 1992. Formation of harzburgite by pervasive melt/rock reaction in the upper mantle. *Nature*, *358*(6388), p.635.

Karato, S.I., 1986. Does partial melting reduce the creep strength of the upper mantle? *Nature*, *319*(6051), p.309.

Lassiter, J.C., Byerly, B.L., Snow, J.E. and Hellebrand, E., 2014. Constraints from Os-isotope variations on the origin of Lena Trough abyssal peridotites and implications for the

composition and evolution of the depleted upper mantle. *Earth and Planetary Science Letters*, *403*, pp.178-187.

Lissenberg, C.J. and Dick, H.J., 2008. Melt–rock reaction in the lower oceanic crust and its implications for the genesis of mid-ocean ridge basalt. *Earth and Planetary Science Letters*, *271*(1-4), pp.311-325.

Liu, C.Z., Snow, J.E., Hellebrand, E., Brügmann, G., Von Der Handt, A., Büchl, A. and Hofmann, A.W., 2008. Ancient, highly heterogeneous mantle beneath Gakkel ridge, Arctic Ocean. *Nature*, *452*(7185), p.311.

Liu, C.Z., Snow, J.E., Brügmann, G., Hellebrand, E. and Hofmann, A.W., 2009. Non-chondritic HSE budget in Earth's upper mantle evidenced by abyssal peridotites from Gakkel ridge (Arctic Ocean). *Earth and Planetary Science Letters*, *283*(1-4), pp.122-132.

Luguet, A. and Reisberg, L., 2016. Highly siderophile element and 187Os signatures in non-cratonic basalt-hosted peridotite xenoliths: Unravelling the origin and evolution of the post-Archean lithospheric mantle. *Reviews in Mineralogy and Geochemistry*, *81*(1), pp.305-367.

Manga, M., 1996. Mixing of heterogeneities in the mantle: effect of viscosity differences. *Geophysical Research Letters*, *23*(4), pp.403-406.

McDonough, W.F. and Sun, S.S., 1995. The composition of the Earth. *Chemical geology*, *120*(3-4), pp.223-253.

Morgan, W.J., 1972. Deep mantle convection plumes and plate motions. *AAPG bulletin*, *56*(2), pp.203-213.

Nakamura, Y. and Tatsumoto, M., 1988. Pb, Nd, and Sr isotopic evidence for a multicomponent source for rocks of Cook-Austral Islands and heterogeneities of mantle plumes. *Geochimica et Cosmochimica Acta*, *52*(12), pp.2909-2924.

Niu, Y., 2004. Bulk-rock major and trace element compositions of abyssal peridotites: implications for mantle melting, melt extraction and post-melting processes beneath mid-ocean ridges. *Journal of Petrology*, *45*(12), pp.2423-2458.

Schiano, P., Burton, K.W., Dupre, B., Birck, J.L., Guille, G. and Allegre, C.J., 2001. Correlated Os–Pb–Nd–Sr isotopes in the Austral–Cook chain basalts: the nature of mantle components in plume sources. *Earth and Planetary Science Letters*, *186*(3), pp.527-537.

Sclater, J.G. and Francheteau, J., 1970. The implications of terrestrial heat flow observations on current tectonic and geochemical models of the crust and upper mantle of the earth. *Geophysical Journal International*, *20*(5), pp.509-542.

Simon, N.S., Neumann, E.R., Bonadiman, C., Coltorti, M., Delpech, G., Grégoire, M. and Widom, E., 2008. Ultra-refractory domains in the oceanic mantle lithosphere sampled as mantle xenoliths at ocean islands. *Journal of Petrology*, *49*(6), pp.1223-1251.

Stracke, A., Snow, J.E., Hellebrand, E., Von Der Handt, A., Bourdon, B., Birbaum, K. and Günther, D., 2011. Abyssal peridotite Hf isotopes identify extreme mantle depletion. *Earth and Planetary Science Letters*, 308(3), pp.359-368.

Suhr, G., Seck, H.A., Shimizu, N., Günther, D. and Jenner, G., 1998. Infiltration of refractory melts into the lowermost oceanic crust: evidence from dunite-and gabbro-hosted clinopyroxenes in the Bay of Islands Ophiolite. *Contributions to Mineralogy and Petrology*, *131*(2-3), pp.136-154.

Sun, C. and Liang, Y., 2014. An assessment of subsolidus re-equilibration on REE distribution among mantle minerals olivine, orthopyroxene, clinopyroxene, and garnet in peridotites. *Chemical Geology*, *372*, pp.80-91.

Sun, S.S. and McDonough, W.S., 1989. Chemical and isotopic systematics of oceanic basalts: implications for mantle composition and processes. *Geological Society, London, Special Publications*, *42*(1), pp.313-345.

Turner, D.L. and Jarrard, R.D., 1982. K-Ar dating of the Cook-Austral island chain: A test of the hot-spot hypothesis. *Journal of Volcanology and Geothermal Research*, *12*(3-4), pp.187-220.

Warren, J.M., 2016. Global variations in abyssal peridotite compositions. *Lithos*, *248*, pp.193-219.

Wood, B.L., 1967. Geology of the Cook Islands. *New Zealand journal of geology and geophysics*, *10*(6), pp.1429-1445.

Wood, C.P., 1978. Petrology of Aitutaki, Cook Islands (Note). *New Zealand journal of geology and geophysics*, *21*(6), pp.761-765.

Workman, R.K. and Hart, S.R., 2005. Major and trace element composition of the depleted MORB mantle (DMM). *Earth and Planetary Science Letters*, *231*(1), pp.53-72.

Zhong, J.Q. and Zhang, J., 2005. Thermal convection with a freely moving top boundary. *Physics of Fluids*, *17*(11), p.115105.

Zhou, M.F., Robinson, P.T. and Bai, W.J., 1994. Formation of podiform chromitites by melt/rock interaction in the upper mantle. *Mineralium Deposita*, *29*(1), pp.98-101.

Zindler, A. and Hart, S., 1986. Chemical geodynamics. *Annual Reviews of Earth and Planetary Sciences*, *14*(1), pp.493-571.

Table 1: Major and trace element abundance data for Aitutaki xenolith and lavas

| Sample+W6: | AK-1008 | AK-1027 | AK-1021 | AK-1023-5 | AK-1017 | AK-1023-4 | AK-1006 | AK-1023-7 | AK-1005 | AK-1023-B | AK-1023-8 | AK-1023-A | AK-1023-6 | AK-1023-1 | AK-1028 | AK-1023-2 | AK-1029 | AK-1023-3 | AK-1026 | AK-1025 | AK-1017R | AK-1020 |
|---|---|---|---|---|---|---|---|---|---|---|---|---|---|---|---|---|---|---|---|---|---|---|
| Lithology | Dunite | Harzburgite | Lherzo | Lherzo | Lherzo | Lherzo | Lherzo | Lherzo | Lherzo | Lherzo | Lherzo | Lherzo | Lherzo | Lherzo | Websterite | Pyroxenite | Pyroxenite | ...id Pyroxenit | Al Pyroxen | Ankaramite | Nephelinite | Alkali Basalt |
| **XRF - Wt. %** | | | | | | | | | | | | | | | | | | | | | | |
| $SiO_2$ | 40.9 | 43.2 | 43.1 | 42.0 | 43.6 | 40.6 | 43.6 | 42.3 | 44.9 | 44.2 | 43.6 | 44.3 | 42.9 | 43.1 | 45.6 | 46.5 | 49.6 | 47.0 | 47.3 | 44.5 | 39.0 | 45.7 |
| $TiO_2$ | 0.01 | 0.08 | 0.07 | 0.19 | 0.12 | 0.16 | 0.16 | 0.17 | 0.03 | 0.20 | 0.11 | 0.20 | 0.22 | 0.39 | 0.41 | 0.62 | 0.58 | 0.80 | 0.99 | 2.03 | 2.78 | 2.04 |
| $Al_2O_3$ | 0.26 | 1.52 | 3.23 | 2.32 | 3.00 | 2.08 | 2.98 | 2.24 | 3.57 | 4.43 | 3.62 | 4.53 | 2.35 | 3.58 | 8.91 | 5.75 | 5.49 | 7.46 | 8.31 | 9.40 | 11.72 | 11.27 |
| $Fe_2O_3T$ | 11.2 | 10.4 | 10.5 | 12.6 | 9.4 | 14.7 | 10.0 | 13.5 | 8.5 | 10.8 | 12.0 | 10.5 | 12.9 | 14.2 | 9.4 | 11.6 | 10.2 | 9.5 | 8.5 | 12.9 | 15.3 | 12.5 |
| $MnO$ | 0.18 | 0.15 | 0.134 | 0.167 | 0.131 | 0.195 | 0.129 | 0.170 | 0.13 | 0.155 | 0.17 | 0.149 | 0.148 | 0.170 | 0.19 | 0.181 | 0.18 | 0.150 | 0.13 | 0.18 | 0.231 | 0.195 |
| $MgO$ | 46.7 | 41.8 | 41.2 | 40.3 | 40.1 | 39.8 | 39.3 | 38.2 | 38.1 | 36.6 | 36.4 | 35.6 | 35.3 | 30.8 | 28.6 | 22.8 | 21.2 | 18.7 | 14.6 | 15.5 | 11.3 | 14.8 |
| $CaO$ | 0.24 | 2.08 | 0.95 | 1.55 | 2.40 | 1.45 | 3.05 | 2.67 | 3.75 | 2.40 | 2.99 | 3.46 | 5.68 | 6.88 | 5.75 | 11.39 | 11.37 | 15.32 | 18.78 | 13.35 | 12.07 | 10.19 |
| $Na_2O$ | 0.06 | 0.12 | 0.09 | 0.21 | 0.61 | 0.20 | 0.42 | 0.19 | 0.15 | 0.39 | 0.21 | 0.49 | 0.28 | 0.43 | 0.44 | 0.55 | 0.63 | 0.69 | 1.18 | 1.22 | 4.85 | 2.01 |
| $K_2O$ | <0.001 | 0.001 | 0.001 | 0.152 | 0.297 | 0.118 | 0.082 | 0.087 | 0.103 | 0.221 | 0.054 | 0.025 | 0.059 | 0.137 | 0.001 | 0.169 | 0.003 | 0.103 | 0.022 | 0.367 | 1.244 | 0.560 |
| $P_2O_5$ | 0.016 | 0.017 | 0.015 | 0.032 | 0.027 | 0.047 | 0.009 | 0.071 | 0.006 | 0.058 | 0.058 | 0.047 | 0.017 | 0.034 | 0.032 | 0.017 | 0.032 | 0.023 | 0.019 | 0.262 | 1.195 | 0.692 |
| Total | 99.60 | 99.31 | 99.26 | 99.55 | 99.73 | 99.30 | 99.63 | 99.55 | 99.21 | 99.43 | 99.22 | 99.33 | 99.76 | 99.65 | 99.29 | 99.54 | 99.34 | 99.73 | 99.82 | 99.84 | 99.70 | 99.88 |
| LOI | 0.38 | 0.58 | 0.88 | 1.12 | 1.27 | 1.36 | 0.83 | 1.47 | 0.32 | 1.29 | 1.99 | 1.51 | 0.37 | 1.53 | 0.92 | 4.06 | 1.02 | 2.74 | 0.99 | 2.30 | 2.70 | 4.07 |
| **XRF - ppm** | | | | | | | | | | | | | | | | | | | | | | |
| Rb | <2 | <2 | <2 | <2 | 48 | <2 | <2 | <2 | <2 | 74 | 37 | <2 | <2 | <2 | 26 | 51 | <2 | 22 | <2 | 9 | 51 | 19 |
| Sr | 10 | 23 | 13 | 17 | 11 | 32 | 42 | 37 | 37 | 13 | 5 | 56 | 10 | 25 | 16 | 13 | 53 | 16 | 93 | 419 | 1389 | 798 |
| Zr | 4 | 6 | 2 | 1 | 11 | 6 | 6 | 8 | 5 | 13 | 5 | 9 | 3 | 6 | 16 | 13 | 9 | 247? | 23 | 120 | 227 | 161 |
| V | 9 | 59 | 64 | 86 | 71 | 88 | 80 | 96 | 91 | 78 | 120 | 85 | 120 | 157 | 150 | 176 | 194 | 247 | 306 | 270 | 204 | 200 |
| Cr | 254 | 2690 | 2990 | 3172 | 2024 | 4175 | 2153 | 3442 | 3780 | 2031 | 2888 | 2484 | 1402 | 2703 | 4078 | 1712 | 2367 | 1475 | 559 | 1087 | 418 | 1076 |
| **ICP-MS - ppm** | | | | | | | | | | | | | | | | | | | | | | |
| Li | 2.0 | 0.4 | 0.7 | 2.2 | 9.7 | 6.3 | 2.8 | 9.4 | 1.4 | 2.0 | 3.3 | 3.9 | 3.9 | 5.4 | 2.0 | 9.6 | 2.0 | 6.3 | 3.6 | 9.6 | 18.4 | 11.6 |
| B | 0.6 | 0.2 | 0.2 | 0.3 | 0.5 | 0.5 | 0.4 | 0.3 | 0.5 | 0.4 | 0.3 | 0.4 | 0.3 | 0.3 | 0.3 | 0.5 | 0.3 | 0.4 | 0.3 | 1.8 | 1.9 | 1.8 |
| Sc | 2.0 | 6.1 | 5.9 | 9.0 | 10.3 | 8.3 | 7.8 | 13.2 | 16.3 | 8.3 | 15.8 | 15.9 | 19.4 | 25.4 | 19.5 | 47.8 | 34.1 | 43.6 | 56.5 | 45.2 | 20.7 | 24.0 |
| Ti | 5.6 | 52.5 | 44.2 | 62.9 | 58.1 | 62.1 | 66.6 | 75.5 | 76.6 | 65.7 | 96.1 | 75.5 | 93.6 | 131.5 | 141.5 | 155.4 | 198.4 | 246.1 | 355.7 | 276.0 | 188.1 | 159.8 |
| V | 177.4 | 566.2 | 453.8 | 1102.4 | 807.5 | 909.3 | 996.3 | 1042.9 | 316.4 | 1204.9 | 741.4 | 1255.0 | 1355.9 | 2291.3 | 2381.1 | 3619.9 | 3558.1 | 4889.6 | 6581.7 | 12240.7 | 16927.6 | 11720.2 |
| Cr | 979.5 | 2644.9 | 2331.5 | 2724.5 | 1747.4 | 3391.5 | 1616.9 | 3074.1 | 2207.2 | 1698.1 | 2619.0 | 2276.4 | 1170.5 | 2262.5 | 3544.1 | 1648.9 | 2396.8 | 1278.3 | 643.3 | 1150.2 | 201.6 | 738.8 |
| Mn | 133.0 | 765.0 | 783.9 | 930.3 | 850.0 | 1172.1 | 753.0 | 1117.9 | 792.7 | 942.0 | 1076.7 | 1008.4 | 932.0 | 1176.9 | 1099.8 | 1162.9 | 1299.4 | 1006.1 | 1030.2 | 1317.8 | 1776.7 | 1349.0 |
| Co | 2416.3 | 96.2 | 97.0 | 104.2 | 96.7 | 123.5 | 98.1 | 110.6 | 79.5 | 95.0 | 108.9 | 95.7 | 104.9 | 102.3 | 72.1 | 78.8 | 63.6 | 60.4 | 43.5 | 70.1 | 62.7 | 67.3 |
| Ni | 5.7 | 1808.6 | 1926.8 | 1898.1 | 1917.7 | 1762.4 | 1967.8 | 1405.8 | 1512.7 | 1575.4 | 1666.4 | 1556.8 | 1378.5 | 1105.6 | 997.2 | 848.8 | 559.8 | 471.2 | 230.5 | 354.2 | 167.0 | 565.3 |
| Cu | 46.1 | 34.3 | 49.9 | 14.9 | 9.5 | 18.3 | 12.4 | 37.3 | 15.4 | 15.1 | 24.9 | 16.2 | 30.8 | 35.7 | 12.0 | 42.5 | 42.5 | 45.2 | 29.2 | 76.8 | 47.5 | 41.8 |
| Zn | 1.684 | 44.2 | 49.9 | 57.2 | 44.8 | 77.1 | 44.4 | 81.2 | 32.5 | 43.1 | 51.8 | 41.2 | 54.0 | 78.9 | 58.5 | 54.8 | 55.5 | 45.7 | 49.0 | 91.8 | 151.0 | 107.1 |
| Ga | 0.987 | 1.874 | 3.095 | 3.675 | 5.011 | 4.047 | 3.630 | 4.052 | 2.475 | 4.163 | 4.248 | 4.072 | 3.189 | 6.037 | 9.908 | 9.251 | 9.063 | 9.952 | 15.734 | 15.520 | 23.257 | 18.924 |
| Ge | 0.807 | 0.754 | 0.849 | 0.921 | 0.830 | 1.031 | 0.852 | 1.029 | 0.742 | 0.910 | 0.982 | 0.910 | 1.049 | 1.145 | 0.947 | 1.191 | 1.191 | 1.222 | 1.734 | 1.570 | 2.508 | 1.656 |
| Rb | 9.579 | 1.153 | 0.785 | 6.946 | 6.943 | 5.375 | 19.270 | 5.539 | 9.168 | 6.055 | 4.845 | 9.794 | 2.906 | 5.074 | 0.679 | 9.442 | 0.858 | 3.443 | 1.398 | 13.573 | 105.027 | 53.889 |
| Sr | 0.196 | 20.472 | 12.563 | 31.532 | 58.138 | 46.883 | 43.856 | 58.778 | 53.397 | 73.748 | 46.097 | 78.003 | 32.102 | 61.866 | 55.315 | 97.003 | 97.662 | 68.290 | 104.992 | 508.336 | 1844.883 | 921.552 |
| Y | 1.076 | 5.087 | 3.327 | 7.651 | 2.849 | 1.919 | 1.717 | 2.058 | 2.034 | 3.459 | 3.426 | 5.371 | 3.245 | 5.067 | 6.611 | 8.071 | 7.283 | 8.071 | 12.959 | 19.691 | 36.128 | 24.605 |
| Zr | 0.370 | 1.671 | 0.884 | 1.894 | 9.469 | 10.885 | 9.113 | 12.258 | 0.303 | 11.986 | 6.984 | 12.215 | 6.787 | 13.482 | 19.500 | 20.265 | 19.709 | 25.139 | 35.040 | 130.523 | 249.842 | 155.567 |
| Nb | 0.038 | 96.2 | 0.027 | 0.312 | 3.494 | 3.027 | 0.819 | 3.469 | 0.268 | 5.279 | 3.687 | 5.152 | 0.985 | 1.324 | 3.930 | 1.969 | 3.916 | 2.110 | 1.806 | 27.451 | 117.910 | 52.381 |
| Mo | 0.238 | 0.058 | 0.818 | 0.266 | 0.093 | 0.232 | 0.203 | 0.830 | 0.077 | 0.332 | 0.170 | 0.262 | 0.324 | 0.279 | 0.079 | 0.135 | 0.283 | 0.820 | 0.064 | 5.039 | 4.745 | 1.080 |
| Sn | 0.044 | 0.334 | 0.025 | 0.106 | 0.293 | 0.260 | 0.203 | 0.289 | 0.217 | 0.253 | 0.240 | 0.294 | 0.044 | 0.346 | 0.376 | 0.506 | 0.488 | 0.601 | 0.064 | 0.708 | 0.854 | 1.523 |
| Cs | 5.275 | 0.053 | 0.201 | 0.106 | 0.306 | 0.155 | 0.328 | 0.114 | 1.321 | 0.036 | 0.084 | 0.132 | 0.084 | 0.179 | 0.029 | 0.109 | 0.031 | 0.048 | 0.049 | 0.380 | 5.139 | 4.150 |
| Ba | 0.346 | 9.846 | 0.041 | 28.841 | 6.943 | 44.050 | 3.805 | 50.598 | 8.999 | 47.692 | 41.799 | 55.945 | 41.799 | 29.953 | 66.030 | 63.831 | 46.425 | 42.138 | 56.040 | 183.726 | 1048.455 | 658.646 |
| La | 0.627 | 1.407 | 0.935 | 1.594 | 2.604 | 2.918 | 1.059 | 4.792 | 0.589 | 4.228 | 3.859 | 4.520 | 1.239 | 3.041 | 4.005 | 4.271 | 5.278 | 4.686 | 4.148 | 22.175 | 46.790 | 48.600 |
| Ce | 0.068 | 3.048 | 1.219 | 3.947 | 4.846 | 6.071 | 2.070 | 8.269 | 0.791 | 7.449 | 7.183 | 8.050 | 2.994 | 5.857 | 8.053 | 12.902 | 13.448 | 9.492 | 10.708 | 46.790 | 212.409 | 82.073 |
| Pr | 0.265 | 0.359 | 0.187 | 0.424 | 0.522 | 0.695 | 0.331 | 0.940 | 0.092 | 0.786 | 0.812 | 0.868 | 0.407 | 0.854 | 1.015 | 1.412 | 1.662 | 1.609 | 1.975 | 5.818 | 21.778 | 9.253 |
| Nd | 0.053 | 1.452 | 0.795 | 1.756 | 2.085 | 2.743 | 1.538 | 3.804 | 0.357 | 3.055 | 3.063 | 3.268 | 1.960 | 3.787 | 4.473 | 6.626 | 6.913 | 7.886 | 10.999 | 23.936 | 79.009 | 37.635 |
| Sm | 0.017 | 0.318 | 0.184 | 0.431 | 0.470 | 0.611 | 0.399 | 0.819 | 0.100 | 0.635 | 0.653 | 0.743 | 0.580 | 1.056 | 1.221 | 1.798 | 1.718 | 2.259 | 3.641 | 5.039 | 15.354 | 7.835 |
| Eu | 0.055 | 0.100 | 0.067 | 0.152 | 0.195 | 0.206 | 0.144 | 0.269 | 0.042 | 0.234 | 0.238 | 0.263 | 0.208 | 0.380 | 0.446 | 0.623 | 0.598 | 0.807 | 1.264 | 1.671 | 4.710 | 2.706 |
| Gd | 0.007 | 0.309 | 0.210 | 0.441 | 0.537 | 0.612 | 0.435 | 0.798 | 0.181 | 0.727 | 0.736 | 0.900 | 0.670 | 1.167 | 1.387 | 1.990 | 1.900 | 2.452 | 3.865 | 5.231 | 14.974 | 7.884 |
| Tb | 0.039 | 0.041 | 0.031 | 0.066 | 0.080 | 0.086 | 0.064 | 0.102 | 0.038 | 0.107 | 0.115 | 0.106 | 0.262 | 0.187 | 0.217 | 0.298 | 0.283 | 0.389 | 0.559 | 0.708 | 4.745 | 1.012 |
| Dy | 0.007 | 0.210 | 0.201 | 0.312 | 0.521 | 0.486 | 0.383 | 0.514 | 0.314 | 0.683 | 0.733 | 0.960 | 0.667 | 1.113 | 1.332 | 1.799 | 1.620 | 2.337 | 3.118 | 4.089 | 8.312 | 5.252 |
| Ho | 0.020 | 0.037 | 0.041 | 0.073 | 0.108 | 0.089 | 0.068 | 0.088 | 0.075 | 0.134 | 0.143 | 0.207 | 0.124 | 0.212 | 0.258 | 0.324 | 0.293 | 0.425 | 0.522 | 0.733 | 1.345 | 0.900 |
| Er | 0.003 | 0.091 | 0.120 | 0.193 | 0.306 | 0.234 | 0.171 | 0.218 | 0.038 | 0.380 | 0.410 | 0.593 | 0.319 | 0.543 | 0.665 | 0.818 | 0.710 | 1.084 | 1.209 | 1.930 | 3.145 | 2.245 |
| Tm | 0.020 | 0.012 | 0.018 | 0.027 | 0.045 | 0.032 | 0.021 | 0.026 | 0.038 | 0.052 | 0.060 | 0.087 | 0.043 | 0.074 | 0.095 | 0.105 | 0.092 | 0.136 | 0.149 | 0.253 | 0.356 | 0.264 |
| Yb | 0.004 | 0.076 | 0.129 | 0.181 | 0.292 | 0.208 | 0.128 | 0.164 | 0.261 | 0.347 | 0.409 | 0.563 | 0.255 | 0.468 | 0.595 | 0.626 | 0.562 | 0.812 | 0.827 | 1.549 | 1.940 | 1.585 |
| Lu | 0.028 | 0.011 | 0.022 | 0.027 | 0.044 | 0.030 | 0.018 | 0.023 | 0.042 | 0.051 | 0.061 | 0.084 | 0.037 | 0.065 | 0.086 | 0.089 | 0.073 | 0.107 | 0.111 | 0.220 | 0.248 | 0.206 |
| Hf | 0.020 | 0.133 | 0.097 | 0.236 | 0.231 | 0.292 | 0.228 | 0.377 | 0.030 | 0.295 | 0.177 | 0.335 | 0.274 | 0.526 | 0.558 | 0.808 | 0.772 | 1.143 | 1.809 | 3.496 | 5.629 | 3.724 |
| Ta | 0.017 | 0.078 | 0.048 | 0.072 | 0.226 | 0.128 | 0.095 | 0.154 | 0.006 | 0.249 | 0.145 | 0.246 | 0.050 | 0.055 | 0.235 | 0.091 | 0.172 | 0.116 | 0.100 | 1.771 | 5.979 | 2.846 |
| W | 0.230 | 0.117 | 0.075 | 0.312 | 0.080 | 0.860 | 0.064 | 0.722 | 0.097 | 0.373 | 0.145 | 0.276 | 0.138 | 0.688 | 0.096 | 0.812 | 0.127 | 0.696 | 0.078 | 0.559 | 0.936 | 0.861 |
| Pb | 0.028 | 0.276 | 0.093 | 0.490 | 0.521 | 1.970 | 0.383 | 2.305 | 0.461 | 0.586 | 1.007 | 0.652 | 1.012 | 1.110 | 0.689 | 5.929 | 1.063 | 1.112 | 0.945 | 1.722 | 11.428 | 4.395 |
| Th | 0.061 | 0.151 | 0.105 | 0.145 | 0.462 | 0.292 | 0.486 | 0.737 | 0.079 | 0.561 | 0.686 | 0.841 | 0.136 | 0.297 | 0.537 | 0.295 | 0.613 | 0.523 | 0.288 | 2.801 | 20.824 | 8.282 |
| U | | 0.056 | 0.029 | 0.087 | 0.165 | 0.156 | 0.025 | 0.202 | 0.049 | 0.188 | 0.167 | 0.189 | 0.051 | 0.120 | 0.080 | 0.155 | 0.097 | 0.133 | 0.054 | 0.629 | 3.713 | 1.478 |

Table 1 (continued)

| | BHVO-2 (n=St Dev | | RSD % | BIR1a (n=2) St Dev | | RSD % | HARZ-01 | St Dev | RSD % | TAB (n=2) |
|---|---|---|---|---|---|---|---|---|---|---|
| Li | 4.8 | 0.3 | 7% | 3.1 | 0.2 | 8% | 0.345 | 0.021 | 6% | 0.0001 |
| B | 1.0 | 0.1 | 7% | 0.3 | 0.0 | 3% | 1.838 | 0.117 | 6% | 0.0774 |
| Sc | 32.0 | 2.2 | 7% | 40.5 | 2.7 | 7% | 3.965 | 0.575 | 14% | 0.3962 |
| Ti | 16300.0 | 961.6 | 6% | 5746.5 | 411.6 | 7% | 12.974 | 1.854 | 14% | 0.0020 |
| V | 317.0 | 19.6 | 6% | 329.7 | 20.5 | 6% | 33.619 | 2.167 | 6% | 0.0471 |
| Cr | 280.0 | 17.1 | 6% | 380.8 | 25.6 | 7% | 2871.468 | 219.410 | 8% | 0.0020 |
| Mn | 1320.0 | 71.7 | 5% | 1356.5 | 79.6 | 6% | 797.891 | 73.252 | 9% | 0.0020 |
| Co | 45.0 | 2.7 | 6% | 54.3 | 3.9 | 7% | 107.175 | 7.552 | 7% | 0.0020 |
| Ni | 119.0 | 6.8 | 6% | 175.6 | 11.4 | 6% | 2350.464 | 151.866 | 6% | 0.0020 |
| Cu | 127.0 | 6.7 | 5% | 118.8 | 6.8 | 6% | 4.253 | 0.467 | 11% | 0.0002 |
| Zn | 103.0 | 2.6 | 3% | 67.8 | 2.4 | 4% | 53.309 | 4.068 | 8% | 1.2786 |
| Ga | 22.0 | 0.8 | 3% | 15.9 | 0.7 | 4% | 0.446 | 0.024 | 5% | 0.0006 |
| Ge | 1.6 | 0.1 | 5% | 1.2 | 0.1 | 4% | 0.865 | 0.073 | 8% | 0.0008 |
| Rb | 9.1 | 0.7 | 7% | 0.1 | 0.0 | 1% | 0.038 | 0.019 | 51% | 0.0002 |
| Sr | 396.0 | 22.1 | 6% | 107.0 | 2.8 | 3% | 0.027 | 0.023 | 85% | 0.0002 |
| Y | 26.0 | 1.0 | 4% | 15.8 | 0.8 | 5% | 0.028 | 0.016 | 58% | 0.0002 |
| Zr | 172.0 | 6.1 | 4% | 15.3 | 0.5 | 4% | 0.649 | 0.043 | 7% | 0.0029 |
| Nb | 18.1 | 0.8 | 4% | 0.5 | 0.0 | 4% | 0.005 | 0.005 | 101% | 0.0002 |
| Mo | 4.0 | 0.2 | 5% | 0.1 | 0.0 | 9% | 0.134 | 0.008 | 6% | 0.0002 |
| Sn | 1.7 | 0.1 | 5% | 1.2 | 0.1 | 4% | 0.284 | 0.060 | 21% | 0.2377 |
| Cs | 0.1 | 0.0 | 13% | 0.0 | 0.0 | 17% | 0.125 | 0.028 | 23% | 0.0001 |
| Ba | 131.0 | 3.0 | 2% | 7.1 | 0.0 | 1% | 0.346 | 0.210 | 61% | 0.0757 |
| La | 15.2 | 0.4 | 2% | 0.6 | 0.0 | 1% | 0.032 | 0.007 | 22% | 0.0002 |
| Ce | 37.5 | 0.8 | 2% | 2.0 | 0.1 | 4% | 0.443 | 0.021 | 5% | 0.0002 |
| Pr | 5.4 | 0.1 | 2% | 0.4 | 0.0 | 3% | 2.432 | 0.189 | 8% | 0.0002 |
| Nd | 24.5 | 0.3 | 1% | 2.4 | 0.0 | 2% | 0.219 | 0.042 | 19% | 0.0002 |
| Sm | 6.1 | 0.1 | 2% | 1.1 | 0.0 | 3% | 0.002 | 0.002 | 111% | 0.0002 |
| Eu | 2.1 | 0.0 | 1% | 0.5 | 0.0 | 1% | 0.001 | 0.001 | 154% | 0.0002 |
| Gd | 6.2 | 0.1 | 2% | 1.7 | 0.0 | 2% | 0.239 | 0.020 | 8% | 0.0002 |
| Tb | 0.9 | 0.0 | 1% | 0.3 | 0.0 | 1% | 0.001 | 0.000 | 34% | 0.0002 |
| Dy | 5.3 | 0.1 | 1% | 2.6 | 0.0 | 0% | 0.003 | 0.002 | 77% | 0.0002 |
| Ho | 1.0 | 0.0 | 2% | 0.6 | 0.0 | 2% | 0.001 | 0.000 | 46% | 0.0002 |
| Er | 2.5 | 0.0 | 1% | 1.7 | 0.0 | 0% | 0.241 | 0.024 | 10% | 0.0002 |
| Tm | 0.3 | 0.0 | 2% | 0.2 | 0.0 | 1% | 0.001 | 0.000 | 17% | 0.0000 |
| Yb | 2.0 | 0.0 | 1% | 1.6 | 0.0 | 0% | 0.011 | 0.001 | 7% | 0.0002 |
| Lu | 0.3 | 0.0 | 2% | 0.2 | 0.0 | 1% | 0.002 | 0.000 | 8% | 0.0000 |
| Hf | 4.4 | 0.1 | 2% | 0.6 | 0.0 | 2% | 0.017 | 0.001 | 7% | 0.0006 |
| Ta | 1.1 | 0.0 | 2% | 0.0 | 0.0 | 1% | 0.003 | 0.001 | 21% | 0.0000 |
| W | 0.2 | 0.0 | 2% | 0.0 | 0.0 | 2% | 6.500 | 0.222 | 3% | 0.0011 |
| Pb | 1.6 | 0.1 | 8% | 5.3 | 0.0 | 1% | 189.325 | 20.143 | 11% | 0.0002 |
| Th | 1.2 | 0.0 | 3% | 0.0 | 0.0 | 0% | 0.002 | 0.000 | 10% | 0.0002 |
| U | 0.4 | 0.0 | 3% | 0.0 | 0.0 | 1% | 0.001 | 0.000 | 11% | 0.0000 |

Table 2: Re-Os isotope and highly siderophile element abundance data for Aitutaki xenoliths and lavas

| Sample | Lithology | | $Al_2O_3$ (wt. %) | MgO (wt. %) | Re | Pd | Pt | Ru | Ir | Os | $^{187}Re/^{188}Os$ | 2σ | $^{187}Os/^{188}Os$ | 2σ |
|---|---|---|---|---|---|---|---|---|---|---|---|---|---|---|
| AK1008 | Dunite | | 0.26 | 46.7 | 0.086 | 6.258 | 5.787 | 7.749 | 3.517 | 1.798 | 0.225 | 0.003 | 0.12368 | 0.00009 |
| AK1027 | Harzburgite | | 1.52 | 41.8 | 0.080 | 6.355 | 10.299 | 6.402 | 3.220 | 2.048 | 0.184 | 0.003 | 0.12974 | 0.00009 |
| AK1006 | Lherzolite | | 2.98 | 39.3 | 0.101 | 4.527 | 3.616 | 3.561 | 1.484 | 2.406 | 0.202 | 0.003 | 0.13171 | 0.00006 |
| AK1023-6 | Lherzolite | | 2.35 | 35.3 | 0.146 | 3.231 | 2.700 | 4.075 | 1.847 | 1.222 | 0.575 | 0.009 | 0.12461 | 0.00009 |
| AK1023-3 | Pyroxenite | | 7.46 | 18.7 | 0.264 | 0.692 | 0.342 | 0.526 | 0.217 | 0.116 | 11.01 | 0.17 | 0.13471 | 0.00019 |
| AK1023-B | Lherzolite | | 4.43 | 36.6 | 0.065 | 2.351 | 4.123 | 4.152 | 2.136 | 0.779 | 0.399 | 0.006 | 0.12923 | 0.00009 |
| AK1017 | Lherzolite | | 3.00 | 40.1 | 0.063 | 3.829 | 3.528 | 4.717 | 2.367 | 2.049 | 0.149 | 0.002 | 0.12505 | 0.00009 |
| AK1023-4 | Lherzolite | | 2.08 | 39.8 | 0.057 | 3.062 | 8.208 | 6.545 | 3.255 | 4.259 | 0.064 | 0.001 | 0.12776 | 0.00010 |
| AK1023-A | Lherzolite | | 4.53 | 35.6 | 0.077 | 2.483 | 4.934 | 5.230 | 2.703 | 0.824 | 0.452 | 0.007 | 0.12799 | 0.00011 |
| AK1023-7 | Lherzolite | | 2.24 | 38.2 | 0.085 | 4.561 | 5.647 | 7.045 | 3.080 | 2.498 | 0.164 | 0.002 | 0.12952 | 0.00007 |
| AK1026 | Gabbro | | 8.31 | 14.6 | 0.052 | 1.660 | 0.238 | 0.196 | 0.039 | 0.049 | 5.13 | 0.08 | 0.13221 | 0.00047 |
| AK1021 | Lherzolite | A split | 3.23 | 41.2 | 0.570 | 0.798 | 2.647 | 2.402 | 1.189 | 0.845 | 3.25 | 0.05 | 0.11849 | 0.00010 |
| AK1021 | Lherzolite | B split | 3.23 | 41.2 | 0.011 | 0.937 | 3.389 | 2.966 | 1.725 | 0.854 | 0.062 | 0.001 | 0.11883 | 0.00006 |
| AK1028 | Websterite | A split | 8.91 | 28.6 | 0.040 | 2.516 | 4.105 | 5.482 | 2.655 | 1.114 | 0.173 | 0.003 | 0.12628 | 0.00007 |
| AK1028 | Websterite | B split | 8.91 | 28.6 | 0.056 | 4.829 | 5.546 | 2.349 | 1.455 | 0.681 | 0.394 | 0.006 | 0.14689 | 0.00012 |
| AK1023-8 | Lherzolite | | 3.62 | 36.4 | 0.035 | 3.730 | 4.564 | 4.141 | 2.096 | 0.531 | 0.322 | 0.005 | 0.12963 | 0.00015 |
| AL1023-2 | Pyroxenite | | 5.75 | 22.8 | 0.196 | 1.122 | 1.119 | 1.044 | 0.563 | 0.325 | 2.90 | 0.04 | 0.12811 | 0.00013 |
| AK1017 L | Nephelinite | | 11.7 | 11.3 | 0.085 | 2.034 | 0.177 | 0.224 | 0.062 | 0.042 | 9.79 | 0.15 | 0.13582 | 0.00023 |
| AK1025 L | Ankaramite | | 9.4 | 15.5 | 0.158 | 1.790 | 1.284 | 0.471 | 0.182 | 0.250 | 3.06 | 0.05 | 0.13673 | 0.00016 |
| MUH-1 Black | SRM | Black Split | | | 0.325 | 9.380 | 10.005 | 7.014 | 5.037 | 3.503 | | | 0.12724 | 0.00008 |
| MUH-1 Blue | SRM | Blue Split | | | 0.204 | 11.769 | 7.970 | 8.472 | 3.717 | 5.311 | 0.185 | 0.003 | 0.12599 | 0.00008 |
| MUH-1 Red | SRM | Red Split | | | 0.215 | 9.721 | 6.916 | 9.767 | 3.740 | 4.688 | 0.221 | 0.003 | 0.12535 | 0.00008 |
| MUH-1 Black | SRM | Black Split | | | 0.207 | 10.390 | 7.487 | 7.326 | 3.468 | 3.581 | 0.278 | 0.004 | 0.12687 | 0.00009 |

Table S1: Total analytical blank values (in pg) and calculated percentages of blanks to samples

| Sample | Re | Pd | Pt | Ru | Ir | Os | $^{187}Os/^{188}Os$ | $2\sigma$ |
|---|---|---|---|---|---|---|---|---|
| TAB 1 | 0.006 | 0.021 | 0.003 | 0.051 | 0.015 | 0.000 | 0.1869 | 0.0065 |
| TAB 2 | 0.003 | 0.021 | 0.003 | 0.059 | 0.012 | 0.000 | 0.1785 | 0.0040 |
| | Blk% Re | Blk% Pd | Blk% Pt | Blk% Ru | Blk% Ir | Blk% Os | | |
| AK-1008 | 3.6% | 1.5% | 0.5% | 0.4% | 0.5% | 0.04% | | |
| AK-1027 | 1.9% | 0.7% | 0.1% | 0.2% | 0.3% | 0.02% | | |
| AK-1006 | 0.5% | 0.8% | 1.0% | 0.5% | 0.4% | 0.10% | | |
| AK-1023-6 | 2.3% | 0.6% | 0.1% | 1.4% | 0.6% | 0.03% | | |
| AK-1023-3 | 1.3% | 3.0% | 0.8% | 11.2% | 5.4% | 0.32% | | |
| AK-1023-B | 5.5% | 0.9% | 0.1% | 1.4% | 0.5% | 0.05% | | |
| AK-1017 | 5.4% | 0.5% | 0.1% | 1.3% | 0.5% | 0.02% | | |
| AK-1023-4 | 6.3% | 0.7% | 0.0% | 0.9% | 0.4% | 0.01% | | |
| AK-1023-A | 4.6% | 0.8% | 0.1% | 1.1% | 0.4% | 0.05% | | |
| AK-1023-7 | 4.2% | 0.5% | 0.0% | 0.8% | 0.4% | 0.02% | | |
| AK-1026 | 6.8% | 1.3% | 1.2% | 30.1% | 29.7% | 0.79% | | |
| AK-1021-A | 0.6% | 2.6% | 0.1% | 2.5% | 1.0% | 0.05% | | |
| AK-1021-B | 0.4% | 0.7% | 0.6% | 0.5% | 0.5% | 0.01% | | |
| AK-1028-A | 0.4% | 0.9% | 0.7% | 0.8% | 0.4% | 0.01% | | |
| AK-1028-B | 6.2% | 0.4% | 0.1% | 2.5% | 0.8% | 0.06% | | |
| AK-1023-8 | 10.0% | 0.6% | 0.1% | 1.4% | 0.6% | 0.07% | | |
| AK-1023-2 | 1.8% | 1.9% | 0.2% | 5.6% | 2.1% | 0.12% | | |
| AK-1017 L | 4.2% | 1.0% | 1.6% | 26.4% | 18.9% | 0.91% | | |
| AK-1025 L | 2.2% | 1.2% | 0.2% | 12.5% | 6.4% | 0.15% | | |

Table S2: Olivine major element chemistry for Aitutaki xenoliths

| Run ID | Sample | MgO | FeO | Al$_2$O$_3$ | CaO | SiO$_2$ | MnO | NiO | Total | Fo content |
|---|---|---|---|---|---|---|---|---|---|---|
| 218 | ,AK1006 1 | 48.96 | 10.42 | 0.05 | 0.08 | 41.12 | 0.12 | 0.39 | 101.1 | 89.33 |
| 219 | ,AK1006 2 | 49.32 | 10.47 | 0.06 | 0.09 | 40.96 | 0.15 | 0.39 | 101.4 | 89.35 |
| 220 | ,AK1006 3 | 48.86 | 10.46 | 0.04 | 0.08 | 41.30 | 0.13 | 0.39 | 101.3 | 89.27 |
| 221 | ,AK1006 4 | 49.26 | 10.09 | 0.04 | 0.08 | 40.28 | 0.11 | 0.40 | 100.2 | 89.69 |
| 222 | ,AK1006 5 | 49.01 | 10.33 | 0.05 | 0.07 | 40.94 | 0.12 | 0.37 | 100.5 | 89.42 |
| 223 | ,AK1006 6 | 49.06 | 10.12 | 0.05 | 0.09 | 40.91 | 0.13 | 0.39 | 100.7 | 89.62 |
| 224 | ,AK1006 7 | 49.22 | 10.38 | 0.05 | 0.07 | 40.76 | 0.15 | 0.37 | 101.0 | 89.42 |
| 225 | ,AK1006 8 | 49.20 | 10.19 | 0.04 | 0.07 | 40.63 | 0.17 | 0.38 | 100.7 | 89.59 |
| 244 | ,AK1028 8 | 47.39 | 11.37 | 0.03 | 0.04 | 40.47 | 0.12 | 0.37 | 99.8 | 88.13 |
| 245 | ,AK1028 9 | 48.11 | 11.32 | 0.01 | 0.04 | 40.53 | 0.12 | 0.31 | 100.5 | 88.33 |
| 247 | ,AK1016 1 | 49.20 | 10.36 | 0.03 | 0.00 | 40.38 | 0.14 | 0.35 | 100.5 | 89.44 |
| 248 | ,AK1016 2 | 49.10 | 10.18 | 0.00 | 0.02 | 40.73 | 0.11 | 0.40 | 100.5 | 89.58 |
| 249 | ,AK1016 3 | 49.46 | 10.04 | 0.01 | 0.00 | 40.46 | 0.14 | 0.39 | 100.5 | 89.77 |
| 250 | ,AK1016 4 | 49.65 | 10.15 | 0.01 | 0.01 | 40.28 | 0.10 | 0.36 | 100.6 | 89.70 |
| 251 | ,AK1016 5 | 49.70 | 10.09 | 0.01 | 0.00 | 40.84 | 0.13 | 0.37 | 101.1 | 89.78 |
| 252 | ,AK1016 6 | 49.64 | 9.95 | 0.02 | 0.00 | 41.05 | 0.13 | 0.38 | 101.2 | 89.89 |
| 253 | ,AK1016 7 | 49.26 | 9.99 | 0.02 | 0.01 | 40.56 | 0.13 | 0.38 | 100.3 | 89.79 |
| 254 | ,AK1016 8 | 49.32 | 10.07 | 0.03 | 0.01 | 40.75 | 0.13 | 0.37 | 100.7 | 89.72 |
| 255 | ,AK1016 9 | 49.42 | 10.02 | 0.01 | 0.01 | 40.85 | 0.14 | 0.42 | 100.9 | 89.78 |
| 256 | ,AK1005 1 | 49.30 | 9.70 | 0.01 | 0.00 | 40.80 | 0.14 | 0.41 | 100.4 | 90.05 |
| 257 | ,AK1005 2 | 49.73 | 9.75 | 0.01 | 0.02 | 40.96 | 0.13 | 0.37 | 101.0 | 90.09 |
| 258 | ,AK1005 3 | 49.66 | 9.64 | 0.00 | 0.01 | 41.11 | 0.10 | 0.39 | 100.9 | 90.18 |
| 259 | ,AK1005 4 | 49.39 | 9.79 | 0.00 | 0.00 | 40.91 | 0.14 | 0.41 | 100.6 | 89.99 |
| 260 | ,AK1005 5 | 49.59 | 9.77 | 0.00 | 0.00 | 40.96 | 0.12 | 0.41 | 100.9 | 90.04 |
| 261 | ,AK1014 1 | 49.35 | 10.10 | 0.03 | 0.07 | 40.48 | 0.09 | 0.34 | 100.5 | 89.70 |
| 262 | ,AK1014 2 | 49.49 | 10.09 | 0.06 | 0.05 | 40.73 | 0.12 | 0.37 | 100.9 | 89.73 |
| 263 | ,AK1014 3 | 49.54 | 10.09 | 0.03 | 0.08 | 40.51 | 0.12 | 0.35 | 100.7 | 89.75 |
| 264 | ,AK1014 4 | 49.04 | 9.84 | 0.04 | 0.06 | 40.90 | 0.13 | 0.38 | 100.4 | 89.88 |
| 265 | ,AK1014 5 | 49.15 | 9.96 | 0.04 | 0.09 | 41.03 | 0.12 | 0.38 | 100.8 | 89.79 |
| 266 | ,AK1017 1 | 49.17 | 9.85 | 0.06 | 0.08 | 41.03 | 0.15 | 0.34 | 100.7 | 89.90 |
| 267 | ,AK1017 2 | 49.44 | 9.82 | 0.06 | 0.04 | 40.39 | 0.14 | 0.35 | 100.2 | 89.97 |
| 268 | ,AK1017 3 | 49.25 | 9.80 | 0.06 | 0.05 | 40.67 | 0.15 | 0.37 | 100.3 | 89.95 |
| 269 | ,AK1017 4 | 50.63 | 9.98 | 0.07 | 0.09 | 41.04 | 0.14 | 0.39 | 102.3 | 90.04 |
| 270 | ,AK1017 5 | 49.22 | 9.84 | 0.04 | 0.07 | 40.91 | 0.12 | 0.40 | 100.6 | 89.91 |
| 271 | ,AK1019 1 | 49.82 | 9.39 | 0.02 | 0.00 | 40.81 | 0.15 | 0.46 | 100.6 | 90.43 |
| 272 | ,AK1019 2 | 49.75 | 9.50 | 0.00 | 0.03 | 40.82 | 0.12 | 0.40 | 100.6 | 90.32 |
| 273 | ,AK1019 3 | 49.27 | 9.58 | 0.00 | 0.00 | 40.71 | 0.11 | 0.37 | 100.0 | 90.16 |
| 274 | ,AK1019 4 | 49.69 | 9.39 | 0.01 | 0.00 | 40.84 | 0.13 | 0.37 | 100.4 | 90.41 |
| 275 | ,AK1019 5 | 49.68 | 9.60 | 0.02 | 0.00 | 41.02 | 0.14 | 0.41 | 100.9 | 90.21 |
| 276 | ,AK1019 6 | 49.96 | 9.58 | 0.01 | 0.00 | 41.21 | 0.15 | 0.41 | 101.3 | 90.28 |

Table S2: Olivine major element chemistry for Aitutaki xenoliths

| Run ID | Sample | MgO | FeO | Al$_2$O$_4$ | CaO | SiO$_3$ | MnO | NiO | Total | Fo content |
|---|---|---|---|---|---|---|---|---|---|---|
| 282.0221 | ,AK1006 9 | 49.75 | 9.51 | 0.02 | 0.02 | 40.87 | 0.13 | 0.39 | 100.7 | 90.31 |
| 283.2666 | ,AK1006 10 | 49.77 | 9.49 | 0.02 | 0.02 | 40.88 | 0.13 | 0.39 | 100.7 | 90.34 |
| 284.5112 | ,AK1006 11 | 49.79 | 9.47 | 0.02 | 0.02 | 40.88 | 0.13 | 0.39 | 100.7 | 90.36 |
| 281 | ,AK1011 5 | 50.00 | 9.32 | 0.02 | 0.01 | 41.03 | 0.12 | 0.38 | 100.9 | 90.53 |
| 282 | ,AK1011 6 | 49.88 | 9.18 | 0.00 | 0.00 | 41.00 | 0.13 | 0.39 | 100.6 | 90.64 |
| 283 | ,AK1011 7 | 50.11 | 9.26 | 0.01 | 0.00 | 40.94 | 0.13 | 0.43 | 100.9 | 90.60 |
| 284 | ,AK1012 1 | 50.16 | 8.99 | 0.00 | 0.00 | 40.75 | 0.09 | 0.41 | 100.4 | 90.86 |
| 285 | ,AK1012 2 | 50.09 | 8.89 | 0.02 | 0.00 | 41.25 | 0.13 | 0.42 | 100.8 | 90.94 |
| 286 | ,AK1012 3 | 50.11 | 8.89 | 0.02 | 0.00 | 40.99 | 0.14 | 0.38 | 100.5 | 90.95 |
| 287 | ,AK1012 4 | 50.16 | 9.26 | 0.00 | 0.01 | 40.88 | 0.10 | 0.36 | 100.8 | 90.61 |
| 288 | ,AK1012 5 | 50.15 | 9.00 | 0.01 | 0.01 | 41.01 | 0.14 | 0.41 | 100.7 | 90.85 |
| 289 | ,AK1012 6 | 50.21 | 9.16 | 0.02 | 0.01 | 40.74 | 0.10 | 0.43 | 100.7 | 90.71 |
| 290 | ,AK1023A | 49.00 | 10.28 | 0.05 | 0.08 | 40.72 | 0.14 | 0.35 | 100.6 | 89.47 |
| 291 | ,AK1023A | 49.22 | 10.20 | 0.04 | 0.06 | 40.65 | 0.12 | 0.40 | 100.7 | 89.59 |
| 292 | ,AK1023A | 48.84 | 10.24 | 0.03 | 0.07 | 40.10 | 0.12 | 0.38 | 99.8 | 89.47 |
| 293 | ,AK1023A | 48.82 | 10.02 | 0.05 | 0.08 | 40.33 | 0.18 | 0.40 | 99.9 | 89.67 |
| 294 | ,AK1023A | 48.85 | 10.18 | 0.05 | 0.08 | 40.99 | 0.15 | 0.38 | 100.7 | 89.53 |
| 295 | ,AK1023A | 48.93 | 10.20 | 0.08 | 0.06 | 40.52 | 0.12 | 0.33 | 100.2 | 89.53 |
| 296 | ,AK1023A | 48.80 | 10.07 | 0.07 | 0.08 | 40.79 | 0.11 | 0.39 | 100.3 | 89.62 |
| 297 | ,AK1023B | 48.37 | 10.86 | 0.03 | 0.07 | 40.53 | 0.15 | 0.36 | 100.4 | 88.81 |
| 298 | ,AK1023B | 49.09 | 10.23 | 0.05 | 0.08 | 40.55 | 0.14 | 0.41 | 100.5 | 89.53 |
| 299 | ,AK1023B | 48.62 | 10.19 | 0.04 | 0.06 | 40.68 | 0.13 | 0.37 | 100.1 | 89.47 |
| 300 | ,AK1023B | 48.79 | 10.29 | 0.07 | 0.08 | 40.84 | 0.15 | 0.38 | 100.6 | 89.42 |
| 301 | ,AK1023B | 48.88 | 10.14 | 0.04 | 0.07 | 40.53 | 0.15 | 0.38 | 100.2 | 89.57 |
| 83 | ,AK1023-B | 49.15 | 10.15 | 0.03 | 0.05 | 40.32 | 0.12 | 0.38 | 100.2 | 89.61 |
| 84 | ,AK1023-B | 48.78 | 10.17 | 0.06 | 0.07 | 40.42 | 0.13 | 0.39 | 100.0 | 89.52 |
| 85 | ,AK1023-B | 48.83 | 10.16 | 0.05 | 0.07 | 40.50 | 0.14 | 0.35 | 100.1 | 89.54 |
| 226 | ,AK1006 9 | 19.72 | 12.03 | 57.24 | 0.00 | 0.08 | 0.10 | 0.38 | 89.6 | 74.49 |
| 227 | ,AK1006 10 | 44.11 | 10.42 | 0.10 | 0.08 | 36.79 | 0.14 | 0.34 | 92.0 | 88.29 |
| 228 | ,AK1021 1 | 33.17 | 6.32 | 4.47 | 0.63 | 55.50 | 0.16 | 0.06 | 100.3 | 90.34 |
| 229 | ,AK1021 2 | 33.19 | 6.20 | 4.38 | 0.61 | 55.44 | 0.14 | 0.06 | 100.0 | 90.51 |
| 230 | ,AK1021 3 | 33.00 | 6.16 | 4.31 | 0.60 | 55.41 | 0.16 | 0.11 | 99.8 | 90.51 |
| 231 | ,AK1021 4 | 32.55 | 6.19 | 4.41 | 0.59 | 55.28 | 0.13 | 0.10 | 99.2 | 90.36 |
| 232 | ,AK1021 5 | 32.70 | 6.18 | 4.73 | 0.59 | 55.16 | 0.13 | 0.11 | 99.6 | 90.41 |
| 233 | ,AK1021 6 | 32.88 | 6.24 | 4.66 | 0.63 | 54.75 | 0.17 | 0.11 | 99.4 | 90.37 |
| 234 | ,AK1021 7 | 33.19 | 6.33 | 4.52 | 0.53 | 55.20 | 0.16 | 0.10 | 100.0 | 90.34 |
| 235 | ,AK1021 8 | 33.24 | 6.12 | 4.49 | 0.57 | 55.52 | 0.15 | 0.07 | 100.2 | 90.64 |
| 236 | ,AK1021 9 | 33.21 | 5.97 | 4.59 | 0.58 | 55.08 | 0.14 | 0.08 | 99.7 | 90.83 |
| 237 | ,AK1028 1 | 32.24 | 7.34 | 4.05 | 0.75 | 54.78 | 0.12 | 0.11 | 99.4 | 88.67 |
| 238 | ,AK1028 2 | 32.24 | 7.14 | 4.03 | 0.74 | 54.95 | 0.11 | 0.12 | 99.3 | 88.95 |
| 239 | ,AK1028 3 | 32.20 | 7.36 | 4.12 | 0.74 | 54.97 | 0.11 | 0.11 | 99.6 | 88.64 |
| 240 | ,AK1028 4 | 32.27 | 7.22 | 3.93 | 0.73 | 54.62 | 0.12 | 0.13 | 99.0 | 88.84 |
| 241 | ,AK1028 5 | 32.52 | 7.27 | 3.99 | 0.76 | 54.98 | 0.15 | 0.08 | 99.8 | 88.85 |
| 242 | ,AK1028 6 | 32.37 | 7.47 | 3.99 | 0.78 | 54.81 | 0.14 | 0.09 | 99.6 | 88.53 |
| 243 | ,AK1028 7 | 32.25 | 7.08 | 4.01 | 0.74 | 55.25 | 0.13 | 0.10 | 99.6 | 89.04 |
| 246 | ,AK1028 10 | 32.36 | 7.26 | 3.98 | 0.77 | 54.80 | 0.10 | 0.11 | 99.4 | 88.81 |